Cerebral Cortex October 2009;19:2248–2268
doi:10.1093/cercor/bhn242
Advance Access publication January 15, 2009

The Electrotonic Structure of Pyramidal Neurons Contributing to Prefrontal Cortical Circuits in Macaque Monkeys Is Significantly Altered in Aging

Doron Kabaso[1,2,3], Patrick J. Coskren[1,2,3], Bruce I. Henry[4], Patrick R. Hof[1,3] and Susan L. Wearne[1,2,3]

[1]Department of Neuroscience, [2]Laboratory of Biomathematics, [3]Computational Neurobiology and Imaging Center, Mount Sinai School of Medicine, New York, NY 10029, USA and [4]Department of Applied Mathematics, School of Mathematics, University of New South Wales, Sydney, Australia

Doron Kabaso and Patrick J. Coskren have contributed equally to this work.

Whereas neuronal numbers are largely preserved in normal aging, subtle morphological changes occur in dendrites and spines, whose electrotonic consequences remain unexplored. We examined age-related morphological alterations in 2 types of pyramidal neurons contributing to working memory circuits in the macaque prefrontal cortex (PFC): neurons in the superior temporal cortex forming "long" projections to the PFC and "local" projection neurons within the PFC. Global dendritic mass homeostasis, measured by 3-dimensional scaling analysis, was conserved with aging in both neuron types. Spine densities, dendrite diameters, lengths, and branching complexity were all significantly reduced in apical dendrites of long projection neurons with aging, but only spine parameters were altered in local projection neurons. Despite these differences, voltage attenuation due to passive electrotonic structure, assuming equivalent cable parameters, was significantly reduced with aging in the apical dendrites of both neuron classes. Confirming the electrotonic analysis, simulated passive back-propagating action potential efficacy was significantly higher in apical but not basal dendrites of old neurons. Unless compensated by changes in passive cable parameters, active membrane properties, or altered synaptic properties, these effects will increase the excitability of pyramidal neurons, compromising the precisely tuned activity required for working memory, ultimately resulting in age-related PFC dysfunction.

Keywords: 3-D morphometry, brain aging, dendritic spines, dendrites, electrotonic properties, pyramidal neurons, working memory

Introduction

Aspects of cognition that are particularly vulnerable in normal aging require information to be held online transiently while processing additional incoming stimuli or manipulating information in some way and involve working memory to varying degrees (Albert 1997; Grady and Craik 2000; Grady et al. 2003; Grady 2008; Stern et al. 2008). In humans and nonhuman primates, cognitive function involving working memory depends critically upon the integrity of circuits in area 46 of the prefrontal cortex (PFC) (Goldman-Rakic 1995, 1996), including local circuits intrinsic to area 46 as well as information projecting from association areas to PFC (for review, see Levy and Goldman-Rakic 2000 and Miller and Cohen 2001). Behavioral studies have shown that old humans (Flicker et al. 1987; Fristoe et al. 1997) and nonhuman primates (Rapp and Amaral 1989; Bachevalier et al. 1991) experience similar cognitive deficits and loss of working memory. Correlated with these cognitive deficits, recent in vitro electrophysiological studies in primate PFC have provided the first indication of age-related biophysical changes at the level of single cells. Luebke et al. (2004) demonstrated significantly higher action potential (AP) firing rates in response to somatic current injections in PFC layers II/III pyramidal cells of old relative to young macaque monkeys (Chang et al. 2005). Because precisely tuned spatial or temporal information is encoded in the persistent firing patterns of PFC neurons during a working memory task (Funahashi et al. 1989; Goldman-Rakic 1995; Miller et al. 1996; and for review, see Fuster 1997), perturbations of normal firing properties in aging may underlie the observed cognitive deficits. Whereas these changes have been well documented by neuropsychological and electrophysiological studies, their cellular substrate remains poorly understood, as neither gross anatomical differences nor neuronal loss have been observed in the primate brain during normal aging (West et al. 1994; Gallagher and Rapp 1997; Gazzaley et al. 1997; Morrison and Hof 1997; Peters et al. 1998; O'Donnell et al. 1999; Hof et al. 2000; Hof and Morrison 2004; Dickstein et al. 2007). This suggests that age-related cognitive changes likely involve more subtle alterations in structure or connectivity, requiring analysis of the intrinsic morphological features of their component neurons at the single cell and subcellular levels of resolution.

We compared the effects of aging on 3-dimensional (3-D) morphology, global mass scaling, and passive electrotonic structure of 2 functionally different classes of pyramidal neurons that contribute to working memory circuits in area 46 of the PFC. These 2 neuron classes are distinguished by their projections: 1) long-range layer III corticocortical projection neurons that send axons from association regions in the superior temporal cortex (STC) to area 46, which we designate in this paper as simply "long projection neurons", and 2) layers II/III pyramidal neurons providing mostly short-range connections among intrinsic groups of pyramidal cells that contribute to local circuits within area 46, which we designate here as "local projection neurons" (Hof et al. 1995; Duan et al. 2003). Previous morphological studies of the effects of normal aging in layers II/III pyramidal cells contributing to these circuits have reported significant reductions in spine densities of both long and local projection neurons, but dendritic structure (lengths and branching complexity) was affected only in long projection neurons (Duan et al. 2003). Because these analyses were conducted essentially in 1-dimension (1-D), ignoring the effects of branch diameters, the present study extends these analyses to include dendritic diameters corrected for the contribution of spine densities and global mass scaling, which are crucial features of the electrotonic structure of individual neurons and their AP firing patterns. In vivo, neuronal firing patterns depend upon complex interactions between passive electrotonic structure, spatial distributions of active channels

and their kinetics, and patterns of synaptic input. Quantitative analysis of the passive electrotonic structure, including the contribution of spine densities, on which these complex interactions are superimposed is the first step in estimating the relative contributions of these interacting factors to altered neuronal firing rates and, ultimately, to altered cognitive function in aging.

We find that aging has significant but different morphological and electrotonic effects in the 2 neuron classes. We also report significant age-related differences in the electrotonic structure of both neuron classes and significant increases in the passive whole-cell input resistance in long projection neurons. Unless compensated by altered synaptic strengths or active or passive cable parameters, these changes in the passive electrotonic structure could be sufficient to explain recently observed increases in single-cell excitability in rhesus monkey PFC during aging (Chang et al. 2005). Despite the regressive dendritic and spine changes, we find that global mass homeostasis, characterized by a fine balance between branching and tapering rates across most of the apical and basal dendrites, is conserved in aging in both long and local projection neurons.

Materials and Methods

Animals, Surgical Procedures, and Tissue Preparation

Materials from a total of 6 young and 5 old monkeys were used in the present study: 3 adult male and 2 adult female long-tailed macaque monkeys (*Macaca fascicularis*, 9–12 years old), 1 adult male rhesus monkey (*Macaca mulatta*, 12 years old), and 2 old male and 3 old female rhesus monkeys (24–25 years old), as previously described (Duan et al. 2003). Body size was 6–10 kg in the young group and 4.5–10 kg in the aged group. All animals were born and raised in captivity and housed in cages for most of their lives. All the aged monkeys included in the present analysis were retired breeders, and none had been involved in any pharmacological or invasive studies. Monthly serological tests, annual physical exams, and necropsy analyses did not reveal any factor that may have influenced the findings obtained in this study. Possible effects of estrogen levels can be ruled out in the old females as both groups included males and females, and all the old females were still cycling at the time of the experiment. Importantly, previous studies of cortical aging that used the same groups of long-tailed and rhesus monkeys in comparison to other macaques species have demonstrated no effect of taxon differences on the outcome of single neuron morphometric analyses (Duan et al. 2003). In addition, a recent evolutionary study of neocortical organization traits among macaques and other primate species clearly supported the close cladistic relatedness of *M. fascicularis* and *M. mulatta* (Van der Gucht et al. 2006). All experimental protocols were conducted according to the National Institutes of Health (NIH) guidelines for animal research and were approved by the Institutional Animal Care and Use Committee at Mount Sinai School of Medicine.

Intracortical injections of fast blue (FB, 4%; Sigma, St Louis, MO) were made into area 46 to identify long and local projection neurons, as described in previous studies (Nimchinsky et al. 1996; Duan et al. 2002, 2003). The animals were perfused intracardially 21 days later. For perfusion, they were deeply anesthetized with ketamine hydrochloride (25 mg/kg) and pentobarbital sodium (20–35 mg/kg i.v.), intubated, and mechanically ventilated. The chest was opened to expose the heart, and 1.5 ml of 0.1% sodium nitrite was injected into the left ventricle. The descending aorta was clamped, and the monkeys were perfused transcardially with cold 1% paraformaldehyde in phosphate-buffered saline (PBS) for 1 min and then for 14 min with cold 4% paraformaldehyde and 0.125% glutaraldehyde in PBS (Duan et al. 2002, 2003).

Following perfusion, 4-mm thick blocks were dissected out of area 46 and the STC, postfixed for 2 h in 4% paraformaldehyde, and cut at 400 μm on a Vibratome. One block of tissue adjacent to the injection sites was used for intracellular injection. FB-labeled cells in this area form local intrinsic horizontal corticocortical projections (called local projections in this study) within area 46 (Pucak et al. 1996; Melchitzky et al. 1998). Another block of tissue used for cell loading was taken from the cortex located in the fundus of the STC, corresponding to areas TPOr, Ipa, and TEa (de Lima et al. 1990). As described in Duan et al. (2002, 2003), the FB-labeled cells visualized in this area formed long association corticocortical projections (referred to as long projections in this study) from the temporal cortex to area 46 (de Lima et al. 1990; Hof et al. 1995). These blocks were postfixed for 2 h in 4% paraformaldehyde and cut at 400 μm on a Vibratome. FB-containing neurons were identified under epifluorescence with a UV filter, impaled, and loaded with 5% Lucifer Yellow (Molecular Probes, Eugene, OR) in dH_2O under a DC current of 3–8 nA for 10–12 min.

The injections of FB in the ventral part of area 46 resulted in comparable numbers of retrogradely labeled local projection neurons within area 46 and the long projection neurons lining the STC. Consistent with previous studies in the macaque monkey PFC (Kritzer and Goldman-Rakic 1995; Pucak et al. 1996), the local projection neurons were located primarily in layers II and III. The long projection neurons formed 2 clearly defined bands, corresponding to layer III and layers V and VI. Only the layers II/III long projection neurons were intracellularly injected with Lucifer Yellow and reconstructed. The final dataset comprised 43 long projection neurons (24 young; 19 old) and 37 local projection neurons (20 young; 17 old), all of which exhibited a typical pyramidal morphology with extensive branching and large numbers of spines, and were reconstructed and used for 3-D analysis. Criteria for inclusion of filled cells for 3-D reconstruction are detailed in Duan et al. (2002).

3-D Neuron Reconstruction and Morphometric Analysis

Neurons were reconstructed using a computer-assisted morphometry system consisting of a Zeiss Axiophot photomicroscope equipped with a Zeiss ZVS-47E video camera system, a Macintosh G3 microcomputer, and custom-designed morphometry software (NeuroZoom) (for details, see Duan et al. 2002, 2003). Neurons were located using a Zeiss Fluar 10× objective and manually drawn using a Zeiss Apochromat 100× objective with a numerical aperture (NA) of 1.4. A live RGB image was ported to the computer screen, and mapping was performed by moving the stage in 1 μm steps through the *z*-axis along the length of each dendrite. Spines were plotted at the same time. In this manner, the *x*, *y*, and *z* coordinates of each dendritic segment, its diameter, and spine locations were recorded to enable later 3-D representation. Dendritic segments from a subgroup of neurons were imaged on a confocal laser scanning microscope (Zeiss LSM 410; Zeiss) to ascertain the quality of cell loading. The NeuroZoom datasets were then exported to generate 3-D renderings of the traced neurons and disconnected branches; abrupt jumps in the *z*-direction and manual errors in dendritic trees were corrected using custom-designed software (Rodriguez et al. 2003; Wearne et al. 2005; Rodriguez et al. 2006). No assessment of tissue shrinkage was performed. Custom code to measure global morphometric parameters summarized in Tables 1 and 2 was written in Matlab (The MathWorks, Natick, MA, Version 6.5). Digitized morphology for each cell in standard neuroanatomical format was imported into Matlab, and the total dendritic length, total dendritic volume, and total number of spines were computed. Overall, spine density (in spines per micrometer of dendritic length) was computed as the total number of spines divided by the total dendritic length. Apical trunk diameter was measured at a distance of 5 μm along the apical trunk from the distal edge of the soma. Reconstructions are available at the Computational Neurobiology and Imaging Center online data repository: http://www.mssm.edu/cnic/repository.html.

3-D Scaling Analysis

The definitions of scaling exponents and methods for fitting them to neuronal data developed in Rothnie et al. (2006) were used. Briefly, scaling exponents were measured in "dendrogram" space, in which

Table 1
Summary statistics for global age-related morphological changes in long projection neurons

Tree	Parameter	Old (n = 19)	Young (n = 24)	% Difference	P
Apical dendrites	Total dendritic volume (μm^3)	692.71 ± 214.76	1215.31 ± 588.74	−43.00	<0.01**
	Total dendritic length (μm)	1801.63 ± 665.88	2625.48 ± 1059.15	−31.38	<0.01**
	Total dendritic surface area (μm^2)	3327.44 ± 1092.98	5075.76 ± 2017.12	−34.44	<0.01**
	Apical trunk diameter (μm)	3.41± 0.78	4.38 ± 1.39	−22.24	<0.01**
	Number of spines	753.32 ± 320.20	1394.33 ± 554.71	−45.97	<0.01**
	Spine density	0.42 ± 0.08	0.54 ± 0.07	−22.39	<0.01**
	Total spine volume (μm^3)	102.19 ± 43.44	189.15 ± 75.25	−45.97	<0.01**
	Total spine surface area (μm^2)	1405.79 ± 498.93	2344.40 ± 974.76	−40.04	<0.01**
Basal dendrites	Total dendritic volume (μm^3)	623.84 ± 192.81	733.39 ± 232.16	−14.94	0.11
	Total dendritic length (μm)	2885.81 ± 946.13	3034.32 ± 556.04	−4.89	0.52
	Total dendritic surface area (μm^2)	4586.34 ± 1469.56	5028.27 ± 1042.31	−8.79	0.28
	Number of spines	1091.37 ± 400.07	1461.29 ± 281.58	−25.31	<0.01**
	Spine density	0.38 ± 0.07	0.48 ± 0.06	−22.37	<0.01**
	Total spine volume (μm^3)	232.27 ± 85.28	311.00 ± 59.93	−25.31	<0.01**
	Total spine surface area (μm^2)	2802.96 ± 847.04	3627.37 ± 734.14	−22.73	<0.01**

Note: Summary statistics for the age-related morphological changes in the total dendritic volume, total dendritic length, total dendritic surface area, apical trunk diameter, number of spines, spine density, total spine volume, and total spine surface area in apical and basal dendrites of long projection neurons. Total dendritic volume does not include spines. Spine densities are reported per micrometer dendritic length. Apical trunk diameter is the diameter of the first cylindrical compartment of apical dendrites, measured 5 μm from the soma. Data are represented as means ± standard deviation. Asterisks indicate statistically significant differences between young and old neurons (*$P < 0.05$; **$P < 0.01$).

Table 2
Summary statistics for global age-related morphological changes in local projection neurons

Tree	Parameter	Old (n = 17)	Young (n = 20)	% Difference	P
Apical dendrites	Total dendritic volume (μm^3)	606.64 ± 182.72	606.48 ± 255.08	0.03	0.99
	Total dendritic length (μm)	1821.45 ± 561.86	1940.46 ± 642.23	−6.13	0.56
	Total dendritic surface area (μm^2)	3233.85 ± 918.53	3399.85 ± 1098.65	−4.88	0.62
	Apical trunk diameter (μm)	3.00 ± 0.91	2.75 ± 0.72	9.72	0.35
	Number of spines	830.35 ± 338.03	1244.10 ± 486.08	−33.26	<0.01**
	Spine density	0.45 ± 0.13	0.63 ± 0.11	−28.40	<0.01**
	Total spine volume (μm^3)	112.64 ± 45.86	168.77 ± 65.94	−33.26	<0.01**
	Total spine surface area (μm^2)	1675.91 ± 1043.83	2065.29 ± 791.31	−18.85	0.22
Basal dendrites	Total dendritic volume (μm^3)	512.41 ± 157.68	505.40 ± 142.80	1.39	0.89
	Total dendritic length (μm)	2439.42 ± 668.54	2329.04 ± 595.18	4.74	0.12
	Total dendritic surface area (μm^2)	3833.70 ± 1078.80	3720.72 ± 964.30	3.04	0.74
	Number of spines	1036.12 ± 266.19	1274.55 ± 379.33	−18.71	0.04*
	Spine density	0.43 ± 0.06	0.55 ± 0.08	−21.20	<0.01**
	Total spine volume (μm^3)	220.51 ± 56.65	271.25 ± 80.73	−18.71	0.03*
	Total spine surface area (μm^2)	2775.06 ± 896.18	3124.32 ± 957.85	−11.18	0.26

Note: Summary statistics for the age-related morphological changes in the total dendritic volume, total dendritic length, total dendritic surface area, apical trunk diameter, number of spines, spine density, total spine volume, and total spine surface area in apical and basal dendrites of local projection neurons. Total dendritic volume does not include spines. Spine densities are reported per micrometer dendritic length. Apical trunk diameter is the diameter of the first cylindrical compartment of apical tree, measured 5 μm from the soma. Data are represented as means ± standard deviation. Asterisks indicate statistically significant differences between young and old neurons (*$P < 0.05$; **$P < 0.01$).

distance is defined as arclength from the soma along dendritic branches, which can be related to the electrotonic structure (Rall 1959, 1962; Rothnie et al. 2006). Four scaling exponents measuring rates of change of mass (d_M), branching (d_N), total cross-sectional area of branches (d_A), and tapering (d_T) with distance from the soma in dendrogram space were defined using the methods described in Rothnie et al. (2006) and outlined in Appendix I. To compute d_M, a constant cytoplasmic density was assumed (see Appendix I).

Apical and basal dendritic trees were separately converted into dendrogram space by dividing them into sections of equal thickness (0.71 μm), separated by parallel planes. The 0.71 μm value was chosen for convenience, based upon dividing the first neuron into 300 equal sections, and was used on later neurons for consistency. Accumulated mass with distance from the soma was calculated within each section by summing the total "cross-sectional area of intersection" of the dendritic structures with each of the parallel planes. Because in dendrogram space, planes are oriented perpendicular to the dendritic axes, these cross-sectional intersection areas were always circular and were computed from the branch diameters at the point of intersection. Total cross-sectional intersection area, number, and average area of intersections with each plane were calculated and each quantity plotted versus distance from the soma in dendrogram space, on a log-log scale. The start and endpoints of the proximal and medial "scaling regions" were determined visually from the log-log plots. In most dendritic trees, 2 scaling regions (linear on a log-log scale), each approximately one-third of the tree, with substantially different slopes, could be clearly identified by eye from the plots of log(number of intersections) and log(average area of intersections). These linear regions comprised a proximal or growth region characterized by steep increases in branching and concomitant reductions in taper (Region I) and a medial or plateau region, in which the slopes of branching and changes in branch diameter were both relatively flat (Region II). The medial scaling regions were abruptly terminated by a third, nonscaling distal region, comprising approximately one-third of a tree (Region III) in which branching decayed rapidly. These natural points of inflection were used to determine the boundaries of proximal and medial regions (for full details, see Rothnie et al. 2006, Fig. 9).

Within these visually identified boundaries, an automated search routine was used to determine more precisely the optimal scaling regions and corresponding fits were performed using the theoretical relationships, $d_M = d_A + 1$ and $d_A = d_N + d_T$ (for their full derivation,

see eqs. A1.6 and A1.7 in Appendix I; Rothnie et al. 2006). Goodness of fit was expressed as an error ε

$$\varepsilon = 1 - \left| \frac{d_M}{d_A + 1} \right| . \quad (1)$$

The best first-order linear fit within each region was found by moving a sliding window covering at least 90% of the size of the region identified by eye, in increments of 1.0 μm from start to end boundaries. The minimum error, ε, identified the optimal scaling region across all 4 log-log plots, subject to 2 further constraints: 1) logarithmic plots of cumulative mass, area, number of intersections, and average area of intersection were all visually linear and 2) the absolute magnitude of the error, ε, was less than 0.3, the maximum value that still allowed good linear fits simultaneously to all 4 log-log data plots. Most neurons exhibited both proximal and medial scaling regions each covering at least one-third of the tree. In some neurons, either the proximal or medial regions were visibly too short to permit reliable fitting. The fitted exponents from these regions were excluded from this analysis. As a result, the effective sample size was reduced (N in Tables 3 and 4).

Including Spines in 3-D Sholl Scaling Analysis

The reconstructed neurons included the 3-D locations of spines but not their geometries. "Representative" spine geometries were estimated separately for apical and basal trees, from high-resolution confocal images of a typical young layer III pyramidal neuron from area 46 using a custom-developed computer-assisted tracing system (VIAS; Rodriguez et al. 2003). The entire neuron was imaged in a mosaic of overlapping tiles, using a ×100 1.4 NA PlanApochromat oil immersion objective lens and scanned at a resolution of 1024 × 1024 pixels, pixel dimensions 0.1 × 0.1 μm, with optical sections collected every 0.08 μm along the z-axis (for details, see Rodriguez et al. 2003). Most spines had identifiable head and neck compartments, from which average dimensions were computed. From a total of 233 apical and 190 basal spines measured, average spine dimensions were head length 0.71 ± 0.01 μm, head diameter 0.47 ± 0.01 μm; neck length 0.44 ± 0.02 μm, neck diameter 0.19 ± 0.01 μm in the apical dendrites and head length 0.82 ± 0.02 μm, head diameter 0.56 ± 0.01 μm; neck length 0.54 ± 0.02 μm, neck diameter 0.16 ± 0.01 μm in the basal dendrites. It was assumed that the spines of long and local projection neurons are similar in size. Because the volume of an average neck compartment was an order of magnitude less than an average head compartment (apical head: 0.12 μm^3; apical neck: 0.012 μm^3; basal head: 0.20 μm^3; and basal neck: 0.011 μm^3), and because most spine necks were below the resolution of the LSM images, only the average dimensions of the head compartments were included in the scaling analysis. The omission of spine necks resulted in a small near-constant reduction in spine mass. Because mass scaling is dependent on the rate of mass change, rather than the particular mass value, the mass scaling was not affected. Each spine head compartment was converted to dendrogram space by aligning its traversed distance in parallel to its parent dendritic branch, and its mass (measured as volume under the assumption of constant density) and area of intersection with the sequential parallel planes were computed along with the rest of the dendritic tree.

Electrotonic Analysis

Electrotonic analysis depends on both the 3-D morphology and the values assumed for passive cable parameters, specific membrane resistance, R_m, cytoplasmic (axial) resistivity, R_a, and membrane capacitance, C_m. In the absence of experimental measurements of these parameters, their values were taken from published electrophysiological measurements in typical neocortical pyramidal neurons. Specific membrane resistance, R_m, was set at 20 $k\Omega cm^2$, cytoplasmic

Table 3

Summary statistics for scaling exponents in long projection neurons with spines

Region	Neuron	Number N	d_M			d_A			d_N			d_T		
			Mean	SD	P	Mean	SD	P	Mean	SD	P	Mean	SD	P
Apical dendrites														
I Proximal	Young	14	0.63	0.12	0.02*	−0.30	0.17	0.08	1.17	0.46	0.76	−1.46	0.40	0.18
	Old	17	0.75	0.13		−0.17	0.21		1.13	0.27		−1.29	0.28	
II Medial	Young	7	0.78	0.12	0.36	−0.29	0.10	0.09	0.11	0.17	0.63	−0.40	0.13	0.04*
	Old	6	0.85	0.15		−0.16	0.14		0.05	0.22		−0.21	0.15	
Basal dendrites														
I Proximal	Young	23	0.85	0.13	0.92	−0.11	0.21	0.97	0.79	0.17	0.48	−0.90	0.23	0.62
	Old	17	0.86	0.12		−0.11	0.19		0.75	0.18		−0.86	0.23	
II Medial	Young	18	1.01	0.16	0.22	−0.11	0.17	0.06	−0.06	0.15	0.001**	−0.05	0.11	0.08
	Old	14	0.94	0.15		−0.23	0.16		−0.25	0.16		0.02	0.09	

Note: Summary statistics for scaling exponents in Regions I (proximal) and II (medial) of apical and basal dendrites of long projection neurons. Means and standard deviations of the scaling exponents d_M, d_A, d_N, and d_T are shown for young and old neurons of long projection type which satisfy the constraints on minimum allowable length of scaling region, linearity of fits, and maximum allowable error, described in the text. Tabulated P values are computed for an independent samples Student's t-tests (*$P < 0.05$; **$P < 0.01$).

Table 4

Summary statistics for scaling exponents in local projection neurons with spines

Region	Neuron	Number N	d_M			d_A			d_N			d_T		
			Mean	SD	P	Mean	SD	P	Mean	SD	P	Mean	SD	P
Apical dendrites														
I Proximal	Young	7	0.78	0.17	0.63	−0.17	0.33	0.49	1.00	0.48	0.37	−1.18	0.54	0.83
	Old	10	0.84	0.25		−0.07	0.30		1.16	0.22		−1.23	0.42	
II Medial	Young	8	0.90	0.19	0.21	−0.17	0.24	0.43	0.02	0.28	0.75	−0.19	0.15	0.64
	Old	7	0.79	0.10		−0.27	0.23		−0.03	0.31		−0.24	0.23	
Basal dendrites														
I Proximal	Young	12	0.92	0.09	0.46	0.05	0.12	0.74	0.82	0.17	0.99	−0.77	0.23	0.83
	Old	13	0.88	0.15		0.03	0.19		0.82	0.25		−0.80	0.30	
II Medial	Young	6	1.09	0.07	0.86	0.02	0.07	0.72	0.01	0.16	0.37	0.01	0.20	0.49
	Old	9	1.11	0.17		−0.02	0.22		−0.08	0.20		0.06	0.11	

Note: Summary statistics for scaling exponents in Regions I (proximal) and II (medial) of apical and basal dendrites of local projection neurons. Means and standard deviations of the scaling exponents d_M, d_A, d_N, and d_T are shown for young and old neurons of local projection type that satisfy the constraints on minimum allowable length of scaling region linearity of fits, and maximum allowable error described in the text. Tabulated P values are computed for an independent samples Student's t-tests (*$P < 0.05$; **$P < 0.01$).

(axial) resistivity, R_a, was set at 150 Ωcm (Stuart and Spruston 1998; Trevelyan and Jack 2002), and C_m was set at 1 μF/cm^2 (Stratford et al. 1989). These passive parameters were held constant for both young and old neurons so that the unique contributions of age-related morphological differences to electrotonic structure could be evaluated. All simulations were performed using the NEURON compartment modeling simulator (Hines 1994). Compartment size and time step were incrementally reduced until further reductions had no effect on the simulation.

Incorporating Spines into Neuron Models

A neuron's electrotonic structure depends critically upon the distribution of surface area. Because spines contribute a substantial portion of that surface area along the dendritic tree, it is important to include their contribution into the dendritic structure before transforming to electrotonic space. We evaluated the contribution to electrotonic structure of reduced spine densities in aging by adjusting the surface area of each dendritic tree according to spine density and average spine dimensions, using the algorithm of Stratford et al. (1989; see also Larkman et al. 1992; Major et al. 1993). For each dendritic branch segment, i, the physical length, l, and diameter, d, of all cylinders in the parent dendritic segment were increased to l' and d' by

$$l' = l \cdot F^{2/3}, \quad (2)$$

$$d' = d \cdot F^{1/3}, \quad (3)$$

where the factor F is the ratio of surface area of segment i including spines to the surface area of segment i without spines. Spines were individually counted for each dendritic segment based on the 3-D spine location data. Because spine geometry data were not available, spine surface areas were computed using the representative apical and basal spine dimensions measured from the typical imaged cell described above and incorporated into the dendrite dimensions using equations (2) and (3). This method preserves the surface area and cytoplasmic (axial) resistivity of each segment i but does not model spine neck resistance; this is appropriate for the present study, which models voltage propagation through dendrites but not into or out of spines. Estimated spine neck dimensions were included in the calculation of spine surface area, despite the limitations of measurement discussed earlier, because the ~10% change in spine area due to their omission would have altered the results to a greater extent than error in the neck measurement.

Whole-Cell Input Resistance, R_N

Whole-cell input resistance to injected currents at the soma, R_N, was computed in 2 ways: 1) analytically from the reconstructed 3-D morphologies of each neuron, using the iterative algorithm of Burke (2000); 2) by simulation: analytic values of R_N were verified against simulated input resistance for each of the 80 reconstructed 3-D morphologies. A series of current steps of duration 200 ms and amplitudes ranging from −120 pA to 80 pA in steps of 20 pA were injected at the soma, somatic membrane potential measured at steady state and plotted against injected current to simulate the passive protocol used in Chang et al. (2005). The slope of this curve was the simulated whole-cell input resistance. The maximum difference in R_N between the 2 methods was 0.4% for either class of neuron.

Voltage Attenuations

The classical concept of electrotonic distance (Rall 1969) has been generalized to account for boundary effects and complex geometries of realistic dendritic trees (Brown et al. 1992; Tsai et al. 1994; Carnevale et al. 1997). By defining the electrotonic metric log attenuation, L_{ij}, as the natural log of voltage attenuation, $A_{ij} = V_i / V_j$, the 3-D structure of a neuron can be mapped from physical to electrotonic space. Thus, $L_{ij} = \ln(A_{ij})$ for signal transfer from point i to point j in the dendritic tree and $L_{ji} = \ln(A_{ji})$ for signal transfer from point j to point i. The property of additivity over a path allows L to be used as a metric for graphical representation of the effects on voltage transfer of a given morphological structure. These "morphoelectrotonic transforms" (Zador et al. 1995) thus encode both anatomical and biophysical features and enable complex functional effects of age-related morphological perturbations to be easily understood via a simple and intuitive visual comparison of young and old transformed trees. Efficient algorithms for computing the electrotonic transforms automatically, developed by Carnevale et al. (1997) and available in the Electrotonic Workbench of NEURON (Hines 1994), were used for both somatopetal (L_{in}) and somatofugal (L_{out}) voltage attenuation transforms.

Spectral analysis of a 19-spike train of APs recorded from the same class of neurons (unpublished data from in vitro recording of layers II/III pyramidal cell from area 46 of a young rhesus monkey, kindly provided by Dr J.I. Luebke of Boston University School of Medicine) demonstrated substantial frequency components up to ~500 Hz. To account for the frequency dependence of voltage attenuation within this biologically relevant range, L_{in} and L_{out} transforms were computed for each neuronal morphology over the full frequency range (DC, 500 Hz). We chose the soma as the reference point for L_{in} and L_{out} transforms. The outward transform thus provides qualitative insight into the effects of somatic spiking on distally located voltage-dependent mechanisms in synaptic plasticity and the inward transform on the ability of synaptic inputs to drive spiking at the soma. To provide a global measure of the efficacy of somatofugal and somatopetal attenuations over an entire dendritic tree and in order to perform statistical analyses of the age-related differences in electrotonic structure in the 2 neuron classes, we computed the mean somatofugal and somatopetal attenuation distances for each cell in the following manner. For each dendritic tree, the logarithm of somatofugal voltage attenuation (L_{out}) was computed from the soma to each dendritic compartment. Taking the mean of these electrotonic distances over the path defined by the entire dendritic tree gave the mean log voltage attenuation in the outward direction, $\bar{L}_{out}$ (for details, see Appendix II). In the inward direction, the somatopetal log voltage attenuation was computed from each dendritic compartment to the soma and then similarly the mean of this quantity was taken over the path length of the dendritic tree, giving the mean log voltage attenuation in the inward direction, $\bar{L}_{in}$. Functionally, these measures provide a single value for each tree, representing the global efficacy of voltage signals propagating from soma to dendritic tips (e.g., backpropagating APs), L_{out}, and the global efficacy of forward propagating voltage signals (e.g., excitatory and inhibitory postsynaptic potentials [EPSPs and IPSPs, respectively]) from distal dendrites to the soma, L_{in}.

Electrotonic analysis was performed both with and without correction for the additional surface areas of spines. To verify that the electrotonic transforms were not affected by the spine-correction method itself, one model neuron of each type was created both with the representative apical and basal spines added explicitly as head and neck compartments at their marked positions along each dendritic branch and with spine-corrected surface areas. Whereas the 2 model types had the same total membrane surface area, the distribution of dendritic surface area was different. The model neuron with spine-corrected surface areas had longer and thicker dendritic branches than the model neuron with spines added explicitly. To compare the electrotonic effects of the 2 models, the anatomical distances from the soma to dendritic segments were normalized by dividing them by the maximum arclength distance to the dendritic tips for each branch. Scatter plots of L_{in} and L_{out} for each dendritic segment were plotted against their respective normalized distance, for each of the 2 models, and the plots overlaid. For each neuron, the overlaid graphs matched closely, demonstrating very similar spatial distributions of voltage attenuation in the 2 methods. As the surface area-corrected models produced a significant speedup in computing the electrotonic transforms, we used this method for including spines in all electrotonic transforms.

Measuring Global Backpropagation Efficacy

Passive AP backpropagation efficacy was measured by simulating injection of a prerecorded AP under voltage clamp at the soma of each of the 80 neuron models, with and without spine correction. The AP was recorded in vitro at the soma of a layers II/III pyramidal cell from area 46 of a young macaque monkey (unpublished data from Dr J. I. Luebke, Boston University School of Medicine). To obtain a global estimate of backpropagation efficacy for each dendritic tree, we computed the maximum backpropagating AP amplitude for each

compartment. To remove the confounding effects of different dendritic lengths, we computed, at each unit of arclength *s* from the soma, the average maximum amplitude across all branches at that distance and finally took the integral of that average over all arclengths, creating a global measure for each apical or basal dendritic tree (for details, see Appendix II). Because this calculation is equivalent to computing the area under a plot of average maximum backpropagating AP amplitude versus dendritic arclength (see Fig. 9) and then normalizing by the maximum dendritic length, we term this measure the normalized backpropagation area ("NBParea," measured in mV).

Statistical Analysis

All statistical comparisons between young and old groups were performed using a Student's *t*-test for independent samples in the case of normally distributed variables and a Wilcoxon rank-sum test for independent samples, if any variable was not normally distributed.

Linear correlations were evaluated using linear regression analysis and the Pearson product moment correlation coefficient. To obtain an interval estimate of the strength of linear relationship, 95% confidence intervals (CI) for the correlation coefficient were computed using the Fisher's z' transformation (Rice 2006). Data were considered statistically significant at $\alpha = 0.05$.

Results

3-D Morphometric Analysis

Tables 1 and 2 show summary statistics for 3-D morphometric analysis of apical and basal dendritic trees of young and old long projection neurons and local projection neurons, respectively. For long projection neurons, all morphometric measures were significantly reduced during aging in the apical dendrites: total dendritic length ($P < 0.01$), total dendritic surface area ($P < 0.01$), total volume ($P < 0.01$), and initial apical trunk diameter ($P < 0.01$). In the basal dendrites of long projection neurons, these measures were also reduced in the old animals but failed to reach statistical significance (Table 1). For local projection neurons, none of these morphometric measures of the dendritic tree were significantly altered by age, either in the apical or basal dendrites (Table 2). For both long and local projection neurons, spine numbers ($P < 0.01$ apical, $P \leqslant 0.04$ basal), spine densities ($P < 0.01$), and total spine volumes ($P < 0.01$ apical, $P \leqslant 0.03$ basal) were significantly reduced in apical and basal dendrites. Total spine surface area was reduced in the apical ($P < 0.01$) and basal dendrites ($P < 0.01$) of long projection neurons only.

3-D Sholl and Scaling Analysis

Figures 1 and 2 compare the spatial distributions of numbers of branch intersections (*A,B*), total cross-sectional branch area with sequential planes at increasing distance from the soma (*C,D*), and average branch diameter (*E,F*), as functions of distance from the soma, in young and old long projection (Fig. 1) and local projection (Fig. 2) neurons. For long projection neurons, branch numbers were significantly reduced in aging only in the medial region (100–200 μm) of the apical dendrites (asterisks, Fig. 1*A*), consistent with a previous 1-D Sholl analysis by Duan et al. (2003). When branch diameters were considered, however, both total branch cross-sectional area (Fig. 1*C*) and average branch diameter (Fig. 1*E*) were significantly reduced in aging over the proximal and medial regions (0–250 μm) of the apical dendrites. Branch numbers (Fig. 1*B*), total branch area (Fig. 1*D*), and average branch diameter were not affected in the basal dendrites of long projection neurons of old monkeys.

Smaller effects of aging were present in the 3-D Sholl analysis of local projection neurons (Fig. 2). Branch numbers were significantly reduced in old monkeys only in the most distal regions (240–300 μm) of the apical dendrites (Fig. 2*A*). A tendency toward increased branching in the middle third of the basal dendrites failed to reach statistical significance (Fig. 2*B*). Total branch cross-sectional area was significantly reduced in aging only at the distal tip of the apical dendrites (Fig. 2*C*) but was not significantly different in the basal dendrites (Fig. 2*D*). Average branch diameters were not altered by age in the apical dendrites (Fig. 2*E*) but were significantly reduced in the mid regions (40–80 μm) of the basal dendrites (Fig. 2*F*). Figures 1 and 2 indicate that not only absolute levels of branching and dendritic volume but also their spatial distributions and rates of change with distance from the soma might vary in aging.

How dendritic mass is distributed with respect to any particular point on the tree is the foundation of morphological contributions to electrotonic structure and hence electrical function in neurons. To evaluate possible effects of age on spatial gradients of branching and mass distribution, we performed a 3-D scaling analysis using techniques developed and validated for neocortical pyramidal neurons (Rothnie et al. 2006).

Scaling exponents measure mass gradients, rather than mass values, relative to distance from the soma and hence are sensitive to spatial distributions of spines rather than absolute spine density. The scaling analysis was performed both with and without spines, producing similar mass scaling results with equivalent statistical significance. Figure 3 and Tables 3 and 4, therefore, report only the scaling exponents measured with the estimated spine masses included. In both long and local projection neurons, aging had no effect on the global pattern of mass distribution, characterized by 2 distinct scaling regions that were present in both apical and basal dendritic trees: a proximal region (Region I, Fig. 3) and a middle region (Region II, Fig. 3), with characteristically different scaling behaviors for mass, branching, and taper, as demonstrated previously for neocortical pyramidal neurons (Rothnie et al. 2006). A distal region (Fig 3, Region III), in which branches rapidly die-off, did not exhibit power-law scaling. Figure 3 shows the raw data with scaling regions (gray shaded areas) from optimized fits of scaling exponents superimposed upon the log-log data plots and upon a dendrogram representation of the basal dendrites of a representative young neuron (Fig. 3*C*) and the apical tree of a typical old neuron (Fig. 3*F*). The raw data in the left and center columns of Figure 3 show log-log plots of total mass (Fig. 3*A1*,*B1*,*D1*,*E1*), total cross-sectional area (Fig. 3*A2*,*B2*,*D2*,*E2*), numbers of branches (Fig. 3*A3*,*B3*,*D3*,*E3*), and average branch diameter (Fig. 3*A4*,*B4*,*D4*,*E4*) versus distance from the soma in dendrogram space. The best-fitting lines have different slopes (d_M, d_A, d_N, and d_T) in Regions I and II, representing characteristically different scaling behaviors. For clarity, only the linear fits of d_N and d_T to proximal scaling regions of apical dendrites are shown in Figure 3.

Summary statistics for differences in scaling exponents between young and old long projection neurons are shown in Table 3 and for local projection neurons in Table 4. In the apical dendrites of long projection neurons, the mass scaling exponent, d_M, was significantly larger ($P = 0.02$) in the proximal regions of old than of young neurons, indicating

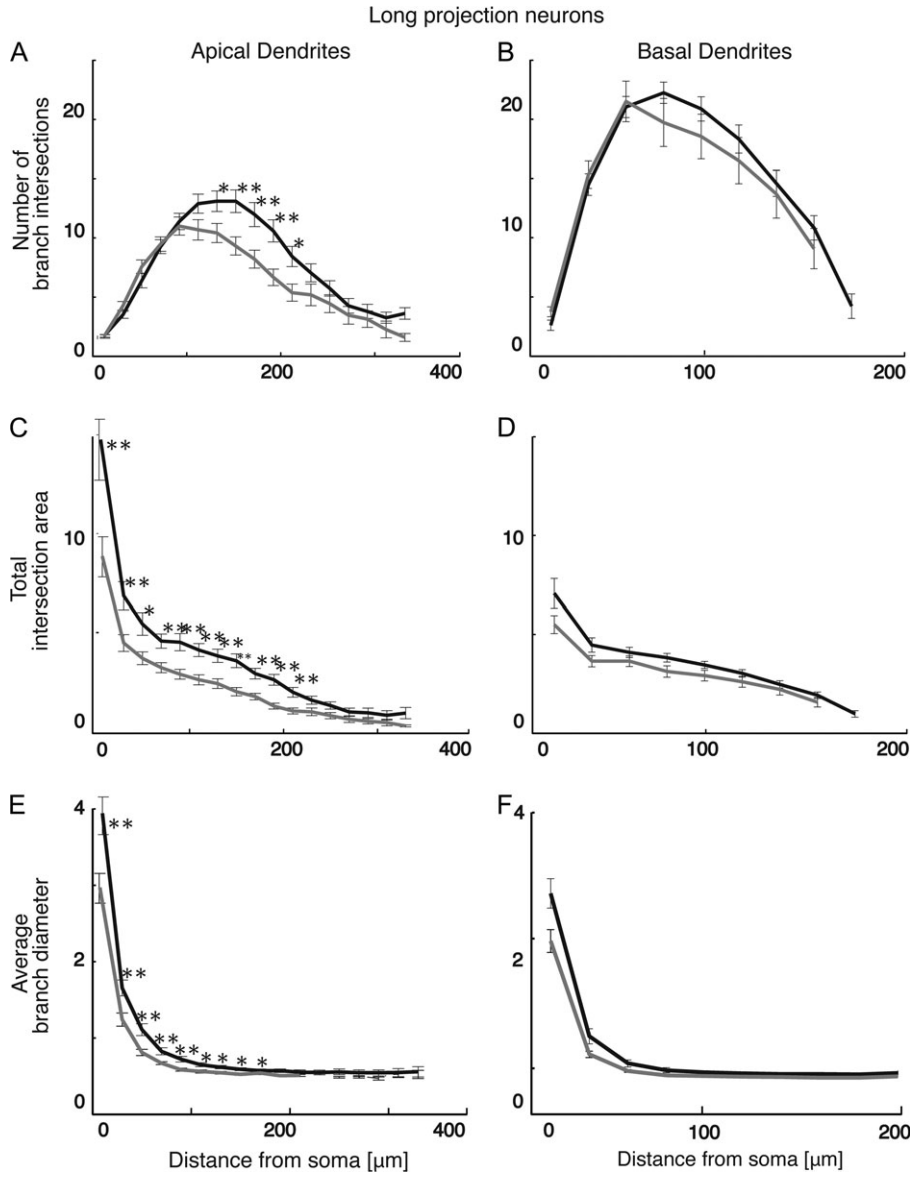

Figure 1. The 3-D Sholl analyses of long projection neurons from young (black lines) and old (gray lines) macaque monkeys in apical (*A*, *C*, *E*) and basal dendrites (*B*, *D*, *F*). Asterisks indicate statistically significant differences across the dendritic tree (*$P < 0.05$; **$P < 0.01$). Values represent means ± standard error of the mean.

a slower rate of decrease in total dendritic mass with distance from the soma (the total area exponent, d_A, smaller with age, approached but did not achieve statistical significance [$P = 0.08$]). This was due primarily to a lower tapering exponent, d_T, which failed to reach statistical significance because of high variability among neurons. In the medial scaling region, variability was less, and the rate of taper was significantly lower in aging ($P = 0.04$). In the basal dendrites, scaling exponents were unaffected by age in the proximal region, but the branching exponent, d_N, was negative and significantly lower in the medial region of old than young long projection neurons ($P < 0.01$), indicating a significantly faster rate of branch die-off with age. Interestingly, this faster branch die-off tended to be compensated by a positive taper or slight "flaring" of individual branches in medial regions of old neurons ($d_T > 0$; Region II, basal dendrites; Table 3), maintaining a relatively uniform mass distribution across proximal and medial scaling regions. For local projection neurons, none of the scaling exponents were significantly different with age in either proximal or medial scaling regions or in apical or basal dendrites (Table 4).

Despite some age-related changes in d_M, d_N, and d_T, the previously reported global mass homeostasis in young long and local projection neurons (Rothnie et al. 2006) was essentially unaffected by aging (compare Fig. 4 of this study with Fig. 11 of Rothnie et al. [2006]). This pattern is summarized in Figure 4 and is characterized as a gradual decrease in total dendritic cross-sectional area with distance from the soma at a constant rate measured by the scaling exponent d_A. The bar graphs in Figure 4 show that d_A, equal to the sum of branching d_N and tapering d_T exponents, maintained a constant, small negative gradient ranging from 0 to –0.30 in both proximal and medial regions of apical dendrites (Fig. 4*A*, first column) and basal dendrites (Fig. 4*B*, first column) for long projection neurons,

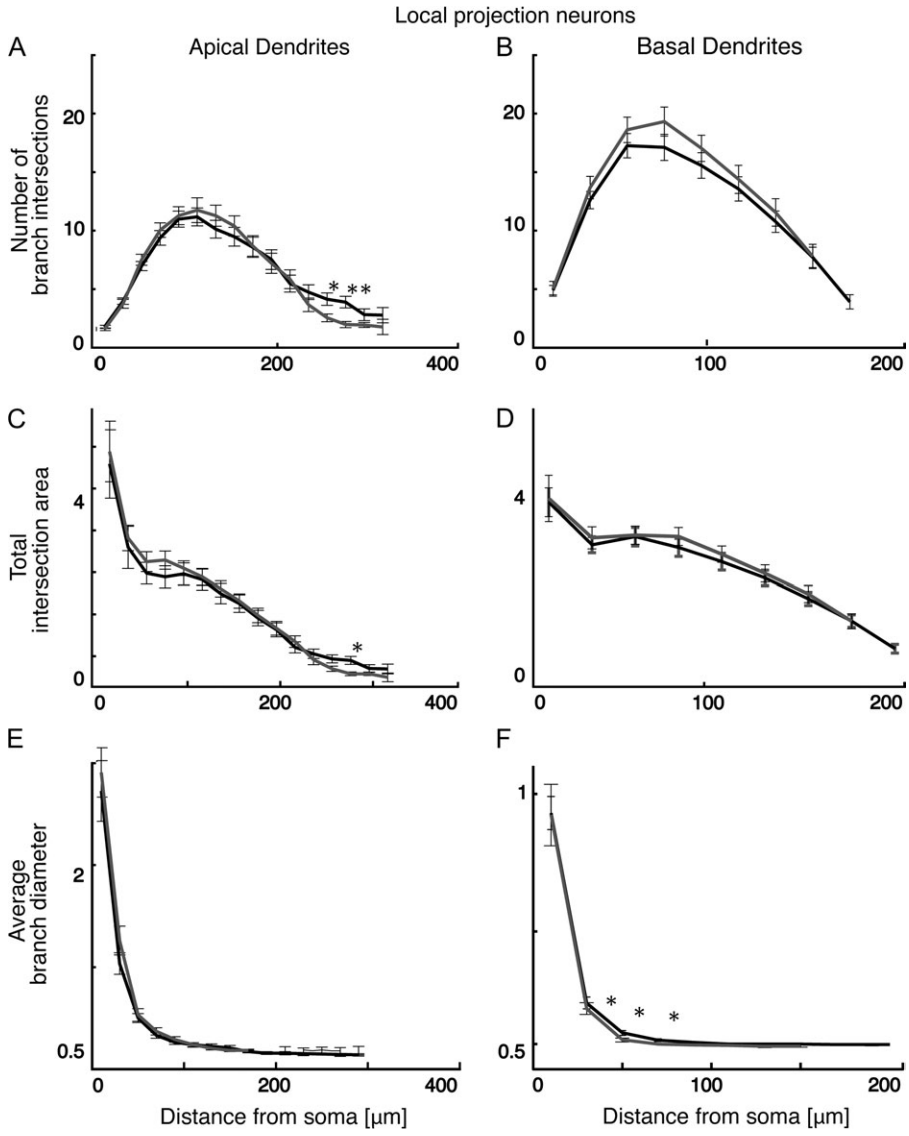

Figure 2. The 3-D Sholl analyses of local projection neurons from young (black lines) and old (gray lines) macaque monkeys in apical (*A*, *C*, *E*) and basal dendrites (*B*, *D*, *F*). Asterisks indicate statistically significant differences across the dendritic tree (*$P < 0.05$). Values represent means ± standard error of the mean.

indicating fairly good cancellation of the positive branching exponent by a negative tapering exponent in each region, proximal and medial. For local projection neurons, d_A was similarly small and negative for both regions of the apical dendrites (Fig. 4*C*, first column) and close to zero in both regions of the basal dendrites (Fig. 4*D*, first column), indicating a slow decrease of total mass with distance from the soma, at an approximately uniform rate. The contributions of branching (d_N) and tapering (d_T) to this mass gradient, however, were different in proximal and medial regions of apical and basal trees. Scaling exponents for young neurons (black bars) and old neurons (gray bars) showed the same homeostatic pattern across the 2 regions. In Region I of the apical trees of long projection neurons, for example, a rapid increase in branching ($\bar{d}_N$ = +1.17 for young; $\bar{d}_N$ = +1.13 for old) was compensated by an even greater tapering rate ($\bar{d}_T$ = −1.46 for young; $\bar{d}_T$ = −1.29 for old), resulting in an overall slightly negative value of d_A ($\bar{d}_A$ = −0.29 for young; $\bar{d}_A$ = −0.16 for old) and hence a global decline in total mass as a function of distance (Fig. 4*A*, top row). In Region II by contrast, the branching and tapering rates were both very low (Fig. 4*A*, second row) but again the exponents d_N and d_T were compensatory, maintaining the same slow negative mass gradient with distance (d_A).

In the apical dendrites, the branching rate d_N in Region II was close to zero for both young and old neurons (Fig. 4*A*,*C*; second row, second column) and slightly negative in the basal dendrites (Fig. 4*B*,*D*; second row, second column), indicating an absence of branching and even a tendency for branches to die-off when $d_N < 0$. The tapering exponent was also small, indicating little change in branch diameters with distance from the soma, either for the apical dendrites (Fig. 4*A*,*C*; second row, third column) or for the basal dendrites (Fig. 4*B*,*D*; second row, third column). When summed to give d_A, these 2 contributions to global mass distribution again almost canceled, resulting in a slow, uniform decrease in mass with distance from the soma, across both Regions I and II.

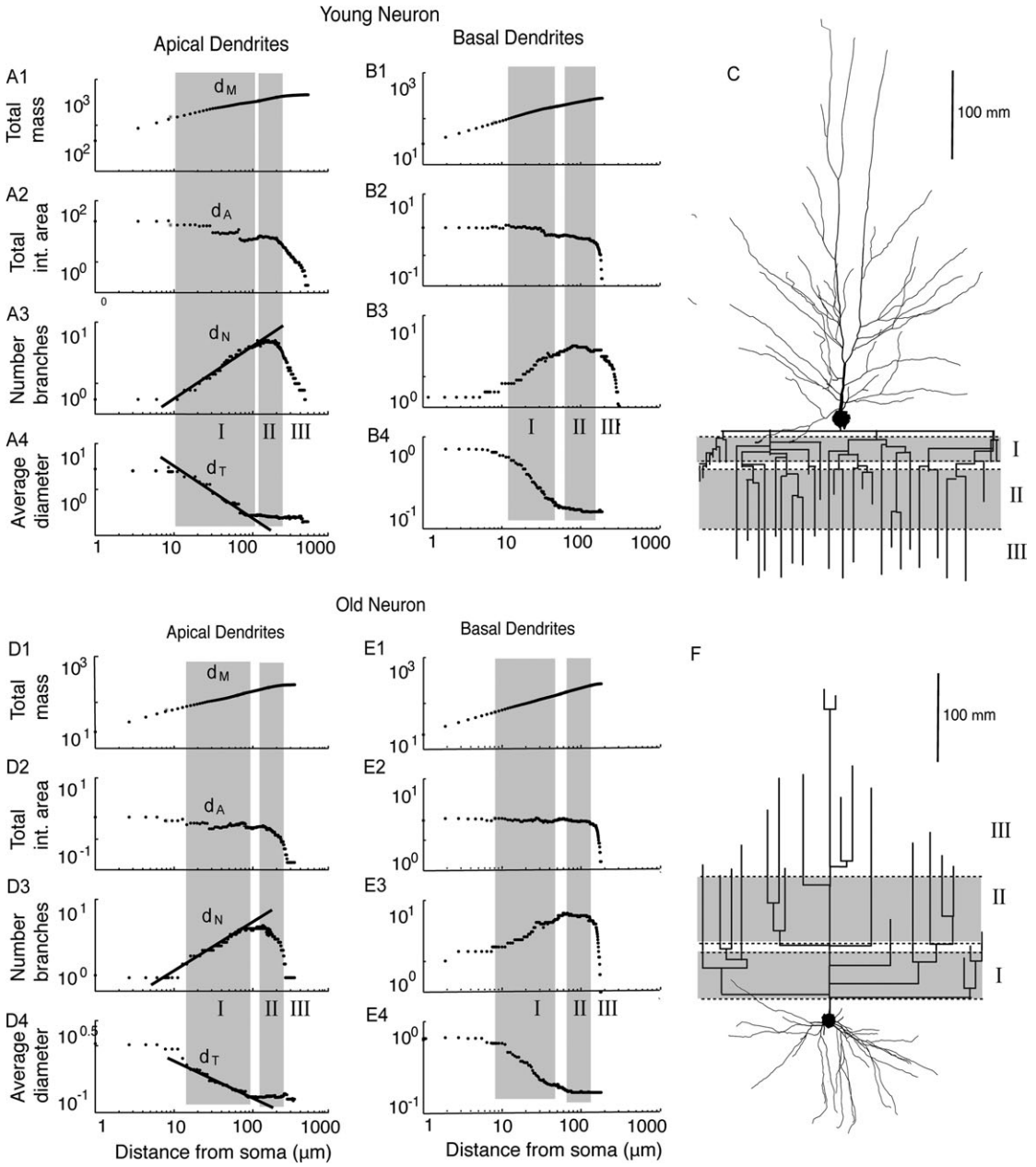

Figure 3. Optimized fits of scaling exponents (black fitted lines, *A3*, *A4*; *D3*, *D4*) and optimal scaling regions (gray shaded bands) for typical young and old long projection neurons. Scaling exponents (d_M, d_A, d_N, and d_T) are fitted on a log-log scale to cumulative mass (*A1*, *B1*, *D1*, *E1*), total area (*A2*, *B2*, *D2*, *E2*), number of branches (*A3, B3, D3, E3*), and average diameter (*A4*, *B4*, *D4*, *E4*) of the intersections with distance from the soma over the proximal (I) and medial (II) regions of basal and apical dendrites. Representative linear fits of d_N and d_T (black lines) in Region I are shown for the apical trees in the young neuron (*A3* and *A4*) and the old neuron (*D3* and *D4*). Two-dimensional projections of 3-D reconstructed young (*C*) and old (*F*) neurons from which the log-log plots were measured. (*C*) The basal tree of the young neuron is represented in dendrogram space, whereas the apical dendrites remain in anatomical space. (*F*) The apical tree of the old neuron is represented in dendrogram space, whereas the basal dendrites remain in anatomical space. Total int. area: total cross-sectional intersection area of branches with sequential parallel planes in dendrogram space. I: proximal scaling region; II: medial scaling region; and III: distal nonscaling die-off region.

Electrotonic Analysis

Electrotonic analysis was performed on 19 old and 24 young long projection neurons and on 17 old and 20 young local projection neurons. The effect of aging on inward and outward mean attenuation lengths ($\bar{L}_{in}$and $\bar{L}_{out}$) was more pronounced in the spine-corrected transforms than in computations based on dendritic parameters alone. Figure 5 shows inward and outward morphoelectrotonic transforms at 0 Hz (DC) of typical spine-corrected young and old long projection (left column, *A–C*) and local projection neurons (right column, *D–F*). In anatomical space, the old long and local projection neurons were both slightly shorter than their young counterparts (top row, Fig. 5*A,D*). Transformation to show outward attenuation exaggerated these differences, primarily in the apical trees (Fig. 5*B,E*). Differences between young and old neurons' attenograms were smaller in the inward attenuation transforms (Fig. 5*C,F*), but again the greatest differences were in the apical

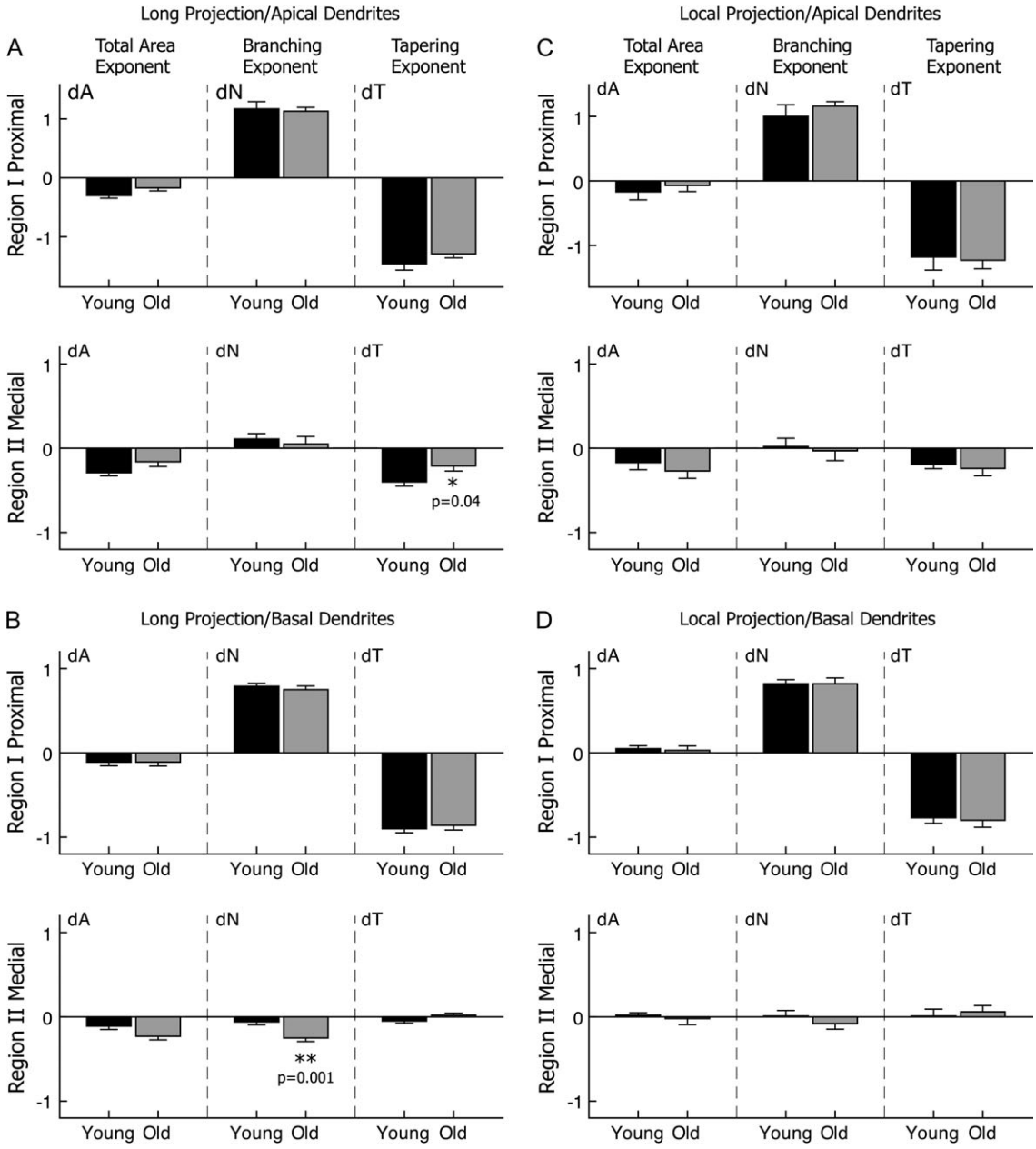

Figure 4. Contributions of branching and tapering exponents to global mass scaling (measured by total area exponent, d_A) in spine-corrected apical (*A*) and basal (*B*) dendrites of long projection neurons and in apical (*C*) and basal (*D*) dendrites of local projection neurons. The 2 rows of panels (*A–D*) contrast the different branching and tapering patterns in Region I (top rows, *A–D*) with Region II (bottom rows, *A–D*). Means ± standard error of the mean are represented as histograms (black, young; gray, old) with superimposed error bars. The asterisks in (*A*, *B*) indicate statistically significant ($P < 0.05$) age-related reductions in tapering and branching exponent of long projection neurons.

dendrites. For each neuron, the inward attenogram was around an order of magnitude larger than the outward attenogram (compare scale bars in Fig. 5*B*,*E* with Fig. 5*C*,*F*). Results of the analysis of mean electrotonic length at 0 Hz are summarized in Figure 6 for long projection neurons and in Figure 7 for local projection neurons.

In long projection neurons, for somatofugal signals (i.e., signals propagating outward from the soma into the dendrites), $\bar{L}_{out}$ of apical dendrites of old neurons was significantly reduced relative to young neurons both when spines were omitted (old, 0.086 ± 0.037; young, 0.12 ± 0.08, $P = 0.045$; Fig. 6*A*, left column) and when spines were included (old, 0.12 ± 0.05; young, 0.17 ± 0.10; $P = 0.02$; Fig. 6*A*, right column). No significant differences in $\bar{L}_{out}$ were present either with ($P = 0.30$) or without including spines ($P = 0.85$) in the basal dendrites (Fig. 6*B*). For somatopetal signals (i.e., signals propagating inward from the dendrites toward the soma), $\bar{L}_{in}$ was significantly reduced in the apical dendrites of old relative to young long projection neurons, whether spines were omitted (old, 1.10 ± 0.25; young, 1.30 ± 0.28; $P = 0.02$; Fig. 6*C*, left column) or included (old, 1.28 ± 0.27; young, 1.54 ± 0.30; $P = 0.006$; Fig. 6*C*, right column). A similar reduction in $\bar{L}_{in}$ was present in aging in the basal trees, becoming significant when spines were included (old, 1.33 ± 0.24; young, 1.47 ± 0.16; $P = 0.03$; Fig. 6*D*, right column) but not significant when spines were omitted ($P = 0.11$; Fig. 6*D*, left column).

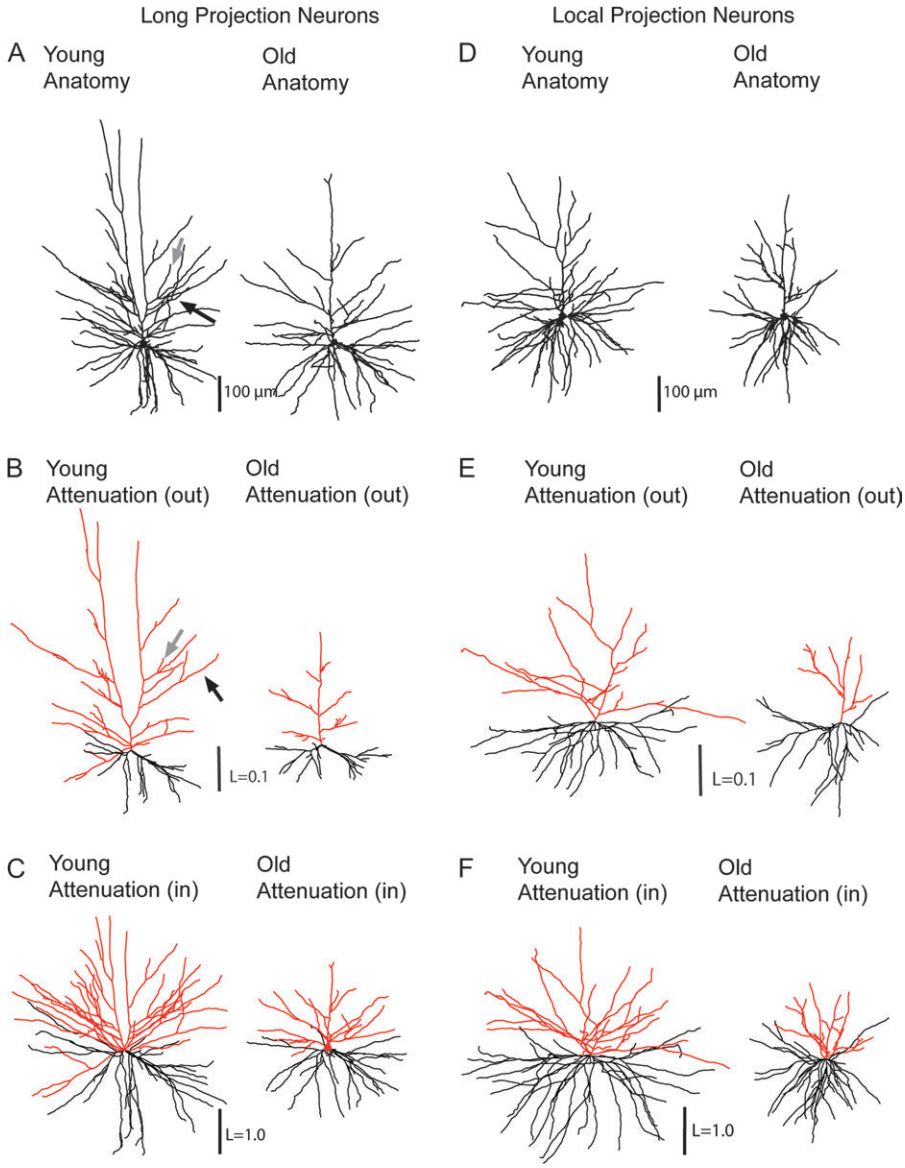

Figure 5. Inward and outward morphoelectrotonic transforms of representative young and old spine-corrected long (*A–C*) and local (*D–F*) projection neurons at 0 Hz. The top row shows anatomical reconstructions of young and old long (*A*) and local (*D*) projection neurons, plotted on the same physical length scales for comparison (black bar representing 100 µm in *A*, *D*). The outward attenuation transforms of these neurons are shown in the second row (*B*, *E*), plotted on the same length scale in attenuation space ($L = 0.1$; black bar). Inward transforms are in the third row (*C*, *F*). In each of the 3 rows, transformed neurons are plotted on the same scale for comparison. Note the increase in scale for inward attenuation transforms ($L = 1.0$; black bar in *C*, *F*) compared with outward attenuation transforms (*B*, *E*). Transformed apical dendrites are shown in red to aid visualization. Individual dendritic sections are affected differently by the transform: examples of relatively larger (black) and smaller (gray) sections are pointed out with arrows in (*A*, *B*).

The pattern of results for inward and outward electrotonic lengths was similar for local projection neurons. In the apical dendrites, $\bar{L}_{out}$ was significantly lower in old than young neurons when spines were included (old, 0.12 ± 0.4; young, 0.17 ± 0.09; $P = 0.02$; Fig. 7*A*, right column), but this difference was not significant when spines were omitted ($P = 0.2$; Wilcoxon rank-sum test). No significant differences in $\bar{L}_{out}$ were present in the basal dendrites, whether spines were omitted ($P = 0.91$) or included ($P = 0.17$; Fig. 7*B*). For somatopetal signals, small reductions in $\bar{L}_{in}$ with aging in the apical dendrites failed to reach significance, either when spine densities were included (old, 1.26 ± 0.22; young, 1.36 ± 0.28; $P = 0.21$; Fig. 7*C*, left column) or when spines were omitted ($P = 0.50$; Fig. 7*C*). No significant age-related differences were present in the basal dendrites of local projection neurons, either with ($P = 0.48$) or without ($P = 0.95$) including spine densities (Fig. 7*D*).

Because the frequency content of a spike train as well as fast EPSPs may have frequency components exceeding 400 Hz (see Methods), L_{in} and L_{out} transforms were computed over the frequency range (0, 500 Hz) at 100 Hz increments. In the apical dendrites of long projection neurons, the mean outward and inward electrotonic lengths $\bar{L}_{out}$ and $\bar{L}_{in}$ were significantly reduced with age over the entire frequency range (Fig. 8*A*,*C*). Interestingly, this age-related reduction became more significant as frequency increased for $\bar{L}_{out}$ (Fig. 8*A*; *P* value decreased from 0.019 at DC to 0.01 at 500 Hz) and remained highly significant with increasing frequency for $\bar{L}_{in}$ (Fig. 8*C*). Similar

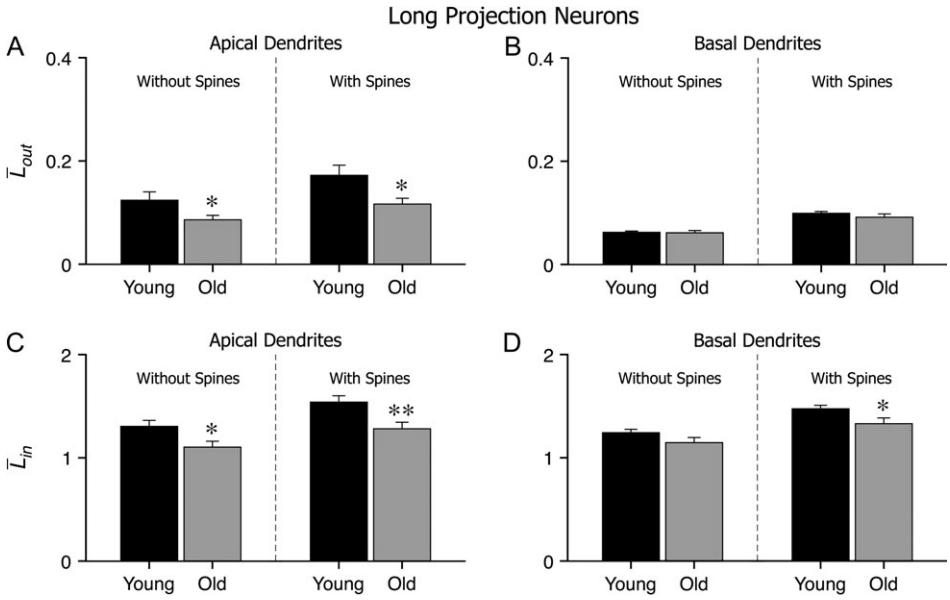

Figure 6. Effects of aging on mean inward ($\bar{L}_{in}$) and outward ($\bar{L}_{out}$) attenuation transforms at DC in long projection neurons. Histograms show means ± standard error of the mean (error bars) of $\bar{L}_{out}$ (*A*, *B*) and $\bar{L}_{in}$ (*C*, *D*) for the young (black bars) and old (gray bars) neuron groups. In each cell (*A–D*), mean attenuation transforms were compared for models without spines (left panels) or including spines (right panels). Asterisks indicate statistically significant differences (*$P < 0.05$; **$P < 0.01$). Values represent means ± standard error of the mean.

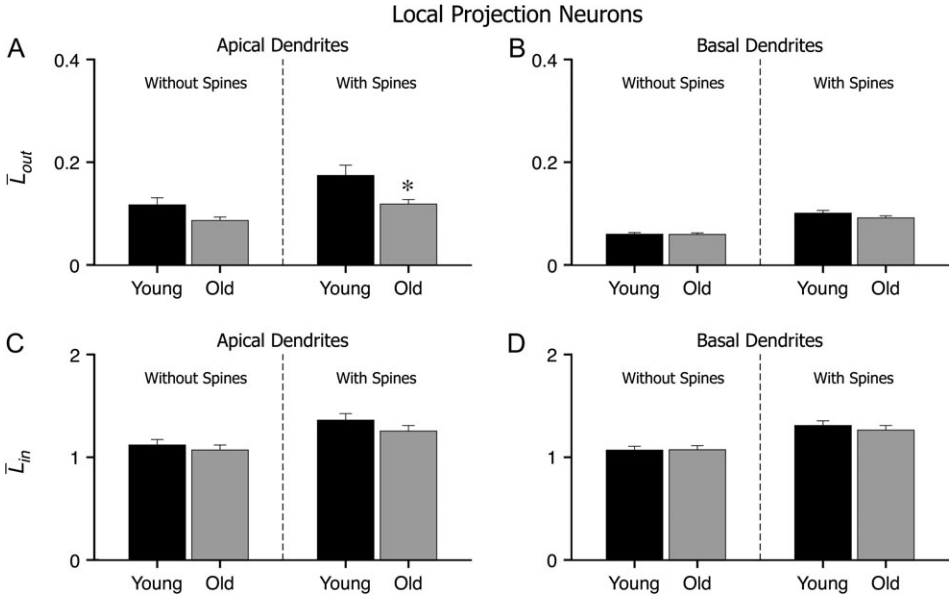

Figure 7. Effects of aging on mean inward ($\bar{L}_{in}$) and outward ($\bar{L}_{out}$) attenuation transforms at DC in local projection neurons. Format as in Figure 6.

age-related reductions in $\bar{L}_{out}$, but not in $\bar{L}_{in}$, were observed for the apical dendrites of local projection neurons (Fig. 8*E,G*). In the basal dendrites, no differences were observed in $\bar{L}_{in}$ or $\bar{L}_{out}$ across the entire frequency range in either long (Fig. 8*B,D*) or local projection neurons (Fig. 8*F,H*).

In long projection neurons, the whole-cell input resistance, R_N, calculated at the soma, was significantly higher in aging, whether spine masses were omitted (old, 234 ± 55 MΩ; young, 192 ± 40 MΩ; $P = 0.009$) or included (old, 186 ± 47 MΩ; young, 145 ± 278 MΩ; $P = 0.002$). For local projection neurons, R_N was not significantly different in aging, either when spines were omitted (old, 256 ± 57 MΩ; young, 255 ± 47 MΩ; $P = 0.98$) or included (old, 199 ± 47 MΩ; young, 187 ± 40; $P = 0.43$).

Simulated AP Backpropagation Efficacy

The functional effects predicted by reduced electrotonic lengths in aging were verified by measuring passive global backpropagation efficacy (normalized backpropagation area: NBParea, see Methods) in response to a simulated AP injected under voltage clamp into the somatic compartment of each reconstructed neuron. For long projection neurons, when spines were omitted from the compartment model, NBParea

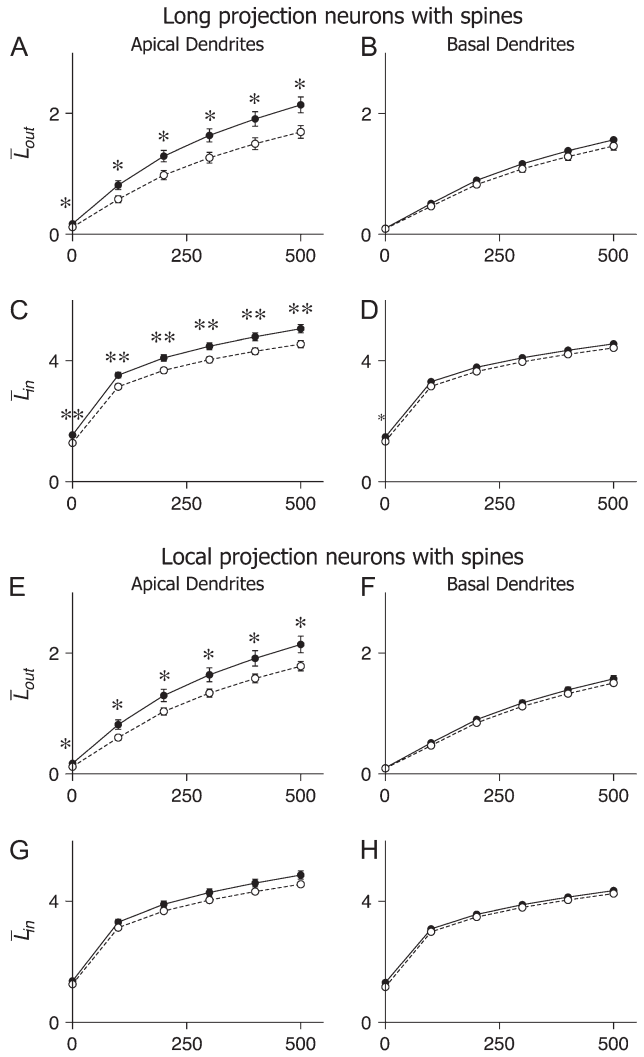

Figure 8. Effect of increasing frequency (0–500 Hz) on $\bar{L}_{in}$ and $\bar{L}_{out}$ transforms in young (solid black line) and old (dashed lines) neurons. Plotted points at each 100 Hz interval represent means ± standard error of the mean. Asterisks indicate statistically significant differences (*$P < 0.05$; **$P < 0.01$). Data series in (H) were virtually identical: aged neuron data have been shifted downward by a value of 0.1 on the log attenuation axis to aid visualization.

was significantly greater in the apical dendrites of old than young neurons (old, 36.0 ± 8.6 mV; young, 30.1 ± 8.1 mV; $P = 0.03$) but not in the basal dendrites (old, 37.4 ± 5.8 mV; young, 36.6 ± 3.1 mV; $P = 0.56$). When spines were included in the model, the significance of this effect increased in the apical dendrites (old, 30.7 ± 7.5 mV; young, 24.5 ± 6.9 mV; $P = 0.01$) but remained not significant in the basal dendrites (old, 30.5 ± 5.1 mV; young, 28.5 ± 2.5 mV; $P = 0.12$).

For local projection neurons with spines omitted from the model, no significant age-related differences in backpropagation efficacy were present, either in the apical dendrites (old, 34.1 ± 5.8 mV; young, 31.1 ± 7.1 mV; $P = 0.16$) or in the basal dendrites (old, 37.9 ± 3.2; young, 37.1 ± 3.1 mV; $P = 0.49$). When spines were included in the model, NBParea was significantly greater in the apical dendrites of old neurons (old, 28.5 ± 5.4 mV; young, 24.5. ± 6.5 mV; $P = 0.049$) but not in the basal dendrites (old, 29.9 ± 3.0 mV; young, 28.0 ± 2.9 mV; $P = 0.06$).

Figure 9 illustrates these age-related differences in global backpropagation efficacy, in response to a simulated somatic AP (Fig. 9*A*, inset), in the apical dendrites of a typical young long projection neuron (Fig. 9*A*) and a typical old long projection neuron (Fig. 9*B*). In response to the same AP profile (inset, Fig. 9*A*), the amplitude of the backpropagating AP falls rapidly in the young neuron, from an initial value of ~75 mV (relative to resting potential) at the base of the apical trunk to a low value of ~10 mV at the distal apical tips (Fig. 9*C*), creating a steep voltage gradient in the color-coded voltages mapped onto the neuronal morphology (Fig. 9*A*). For the old neuron, the same somatic AP created a shallower voltage gradient from apical trunk to distal tips, falling from ~75 to ~30 mV (Fig. 9*D*), resulting in a higher global backpropagation efficacy throughout the tree and a higher value of NBParea (Fig. 9*B*, inset).

The predictive value of the electrotonic measures $\bar{L}_{out}$ and R_N was compared with traditional global morphometric parameters of dendritic structure (total dendritic length, total dendritic surface area, total volume) within the apical dendrites of all neurons with spines included. Comparisons of correlations of NBParea with $\bar{L}_{out}$, R_N at base of the apical trunk (Fig. 10*B*), and total dendritic surface area (Fig. 10*C*) in the apical dendrites of all neurons showed that $\bar{L}_{out}$ was the best linear predictor of passive global backpropagation efficacy, with a correlation coefficient of $r = -0.87$ and a 95% CI for the correlation coefficient, CI(r), of (–0.81, –0.92). When NBParea versus $\bar{L}_{out}$ were plotted on a log-log scale, the correlation coefficient rose to $r = -0.95$, CI(r) = (–0.93, –0.97) (Fig. 10*A*; and see Appendix II for a formal explanation). Input resistance R_N at the base of the apical trunk correlated positively, but more weakly, with NBParea ($r = 0.42$, 95% CI[r] = [0.22, 0.58]). The traditional morphometric measures were only weakly related to NBParea (total dendritic surface area: $r = -0.67$, 95% CI(r) = [–0.52, –0.77], total dendritic volume: $r = -0.39$, CI(r) = [–0.19, –0.56]).

Discussion

This study was designed to compare the effects of aging on 3-D morphology, global mass scaling, and passive electrotonic structure of 2 functionally different populations of pyramidal neurons that contribute to working memory circuits in PFC area 46. We demonstrate significant, functionally relevant 3-D structural alterations in normal aging for both neuron types that cannot be observed using standard 1-D or 2-D morphometric analyses. Specifically, when dendritic diameters, rates of taper, and spine masses were accounted for, functionally significant alterations in the electrotonic structure of both long and local projection neurons were revealed. This result contrasts with previous morphometric studies, which have reported significant alterations in dendritic branching structure only in long projection but not in local projection neurons (Duan et al. 2000, 2003).

Anatomical and Functional Differences between Long and Local Projection Neurons

Anatomical studies in macaque monkeys have demonstrated that local projection neurons in the PFC extend horizontal axon collaterals that terminate in a regular pattern of stripes or microcolumns 200–400 μm wide, restricted to cortical layers I–III (Levitt et al. 1993; Pucak et al. 1996; and for review, see Lewis et al. 2002). The somata of local projection neurons are arranged in similar vertical stripes that overlap the stripes of axon terminals (Pucak et al. 1996), suggesting that reciprocal

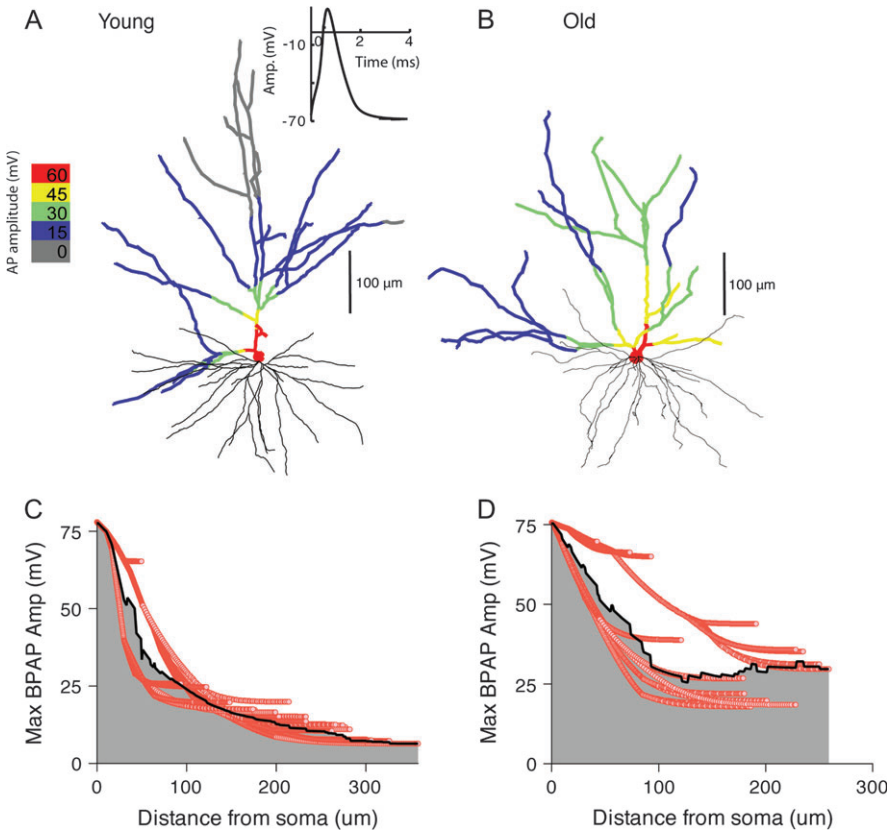

Figure 9. Simulated passive AP backpropagation in apical dendrites of representative young (*A*) and old (*B*) long projection neurons. (*A*, *B*) Reconstructed morphology of each cell is shown above, with superimposed color map representing peak voltage (relative to resting potential of −65 mV) attained by the backpropagating AP injected under voltage clamp at the soma, according to the color scale shown at left. The somatic AP is shown in the inset (*A*). (*C*, *D*) Maximum backpropagating AP amplitudes (relative to −65 mV) attained in each apical branch segment (red curves) are plotted against the distance in dendrogram space from the soma for young (*C*) and old (*D*) neurons. The black curve describes the mean maximum backpropagating AP amplitude computed at each distance from the soma. Normalized backpropagation area (NBParea, shown as gray region) was computed as described in the text.

connections between functionally related stripes (Kritzer and Goldman-Rakic 1995; Melchitzky et al. 1998) might provide a neural substrate for the recurrent excitatory networks believed to subserve the delay-related persistent activity (Funahashi and Kubota 1994; Lisman et al. 1998; Durstewitz et al. 2000; Wang 2001) that underlies working memory in the PFC (Goldman-Rakic 1988, 1995; Miller et al. 1996; Miller and Cohen 2001). The long projection neurons are predominantly layer III pyramidal neurons (Barbas 1986; Hof et al. 1995), exhibit a different neurochemical phenotype from those providing local projections (Hof et al. 1995), and represent a particularly vulnerable class of neurons in Alzheimer's disease (Hof et al. 1990; Bussière et al. 2003; Hof and Morrison 2004). Functionally, long corticocortical projection neurons transmit increasingly complex sensory or motor information along hierarchies of organized cortical regions, linking distant and functionally different regions of the cerebral cortex, whereas local projection neurons subserve lattices of connections within a given cortical region and may enable local binding of converging information within a given cortical domain (Barbas 1986; Goldman-Rakic 1995; Hof et al. 1995; Lewis et al. 2002).

Effects of Aging on 3-D Morphometric Measures, Mass Scaling, and Global Mass Homeostasis

In long projection neurons, standard 3-D morphometry revealed similar significant reductions in branching complexity of apical but not basal dendrites with age, as previously observed in 1-D and 2-D studies (de Brabander et al. 1998; Duan et al. 2003; Shimada et al. 2006). The addition of spines to the dendritic mass simply amplified this difference, resulting in highly significant reductions in total dendritic mass over the proximal and middle thirds of the apical but not the basal trees. Although standard morphometric analysis found no significant age-related differences in the dendritic morphology of local projection neurons, suggesting that the electrotonic structure of these neurons might also be unchanged, inclusion of spine surface areas and the reciprocal interaction of length and diameter in computing the electrotonic transform revealed functionally significant changes in electrotonic structure.

We observed statistically significant reductions in the primary trunk diameter, total dendritic length, total dendritic volume, and total dendritic surface area of apical dendrites in long projection neurons during aging, whereas no significant changes in any of those metrics were observed in the apical tree of local projection neurons. The shorter total apical lengths in long projection cells with aging resulted primarily from significant reductions in the number of terminal and parent branches and significantly shorter mean lengths of parent branches. In accordance with previous 1-D studies (Duan et al. 2003), the total number of spines and spine density were significantly reduced on basal and apical dendrites of both long and local projection neurons. However, due to the

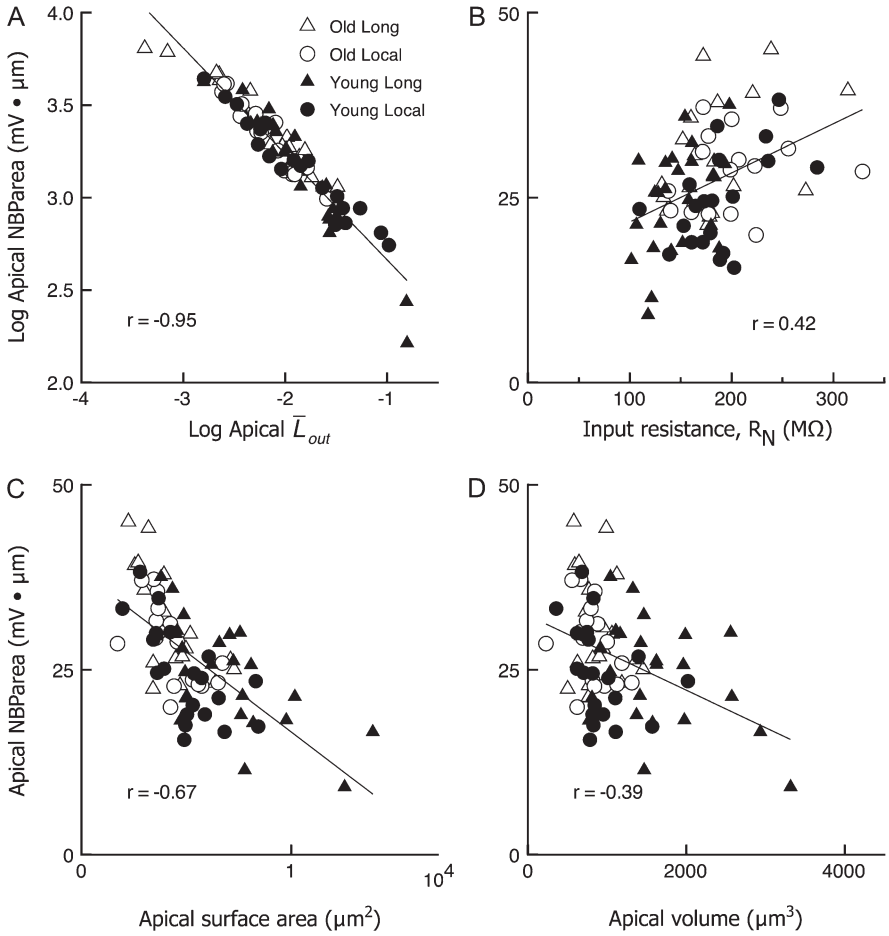

Figure 10. Comparison of traditional morphometric measures, total surface area and total volume, as predictors of backpropagation efficacy (NBParea), with electrotonic measures. NBParea is plotted as a scatterplot versus each of the predictive variables, and the best-fitting first-order regression line superimposed. (*A*) The electrotonic measure $\bar{L}_{out}$ is the best predictor of NBParea, with a strong linear negative correlation that becomes even stronger on a log-log scale. (*B*) Input resistance at the base of the apical trunk, R_N, showed a moderate, positive correlation; (*C*) total surface area showed a moderate, negative correlation; and (*D*) total volume was poorly correlated with backpropagation efficacy.

limitations of manual tracing methods (for details, see Duan et al. 2003), those measurements represented estimates rather than absolute values because some dendritic processes were cut or distorted during tissue sectioning. Most importantly, spines located directly above or below a dendritic branch and spines oriented along the optic axis when focusing through the tissue are extremely difficult to detect manually under light microscopy, leading to substantially underestimated spine counts (Duan et al. 2003; Rodriguez et al. 2008).

The spatial complexity of dendritic branching patterns has traditionally been measured in 2D, using standard Sholl analysis (Sholl 1953) or fractal analyses both in 2D (Smith et al. 1989; Jelinek and Elston 2001) and in 3-D (Caserta et al. 1995; Henry et al. 2002). In these studies, "complexity" was quantified by a power law scaling exponent describing the rate of increase or decrease of branch numbers with distance from the soma over substantial regions of the tree. Recently, we showed that the scaling exponent describing global mass distribution, d_M, can be decomposed into a sum of 2 independent scaling exponents representing branching rates (d_N) and tapering rates (d_T) over prescribed scaling regions of the dendritic tree. These scaling exponents were related to the electrotonic structure of the neuron (Rothnie et al. 2006). The scaling regions were robust in both long and local projection neurons and exhibited a distinctive homeostatic pattern of mass distribution: exponents characterizing branching (d_N) and tapering (d_T) rates in each scaling region were inversely related in a fine balance that maintained a constant spatial gradient (d_A) across both proximal and medial regions of the dendritic tree. This pattern was interpreted as a form of global mass homeostasis in which the conserved quantity was the spatial gradient of dendritic mass with distance from the soma (Rothnie et al. 2006).

Although aging did not alter specific scaling exponents in local projection neurons, long projection neurons exhibited less taper (d_T) in apical dendrites and greater branch die-off (d_N) in medial regions of basal dendrites. Given these changes, together with the highly significant loss of spines and reduction of dendritic diameters in the old animals, one might expect the global mass homeostasis to be lost in old neurons. Remarkably, despite significant changes in specific indices of branching and tapering, these measures remained compensatory within each scaling region, such that the global spatial gradient of mass distribution was unchanged by aging in either neuron class. An analogous form of mass homeostasis, in which the conserved quantity was total dendritic size, was reported recently by Samsonovich and Ascoli (2006). In a morphometric meta-analysis

of many different types of pyramidal neurons, they demonstrated that alterations in dendritic size in one part of a dendritic tree are compensated by the remaining dendrites in the rest of the cell. This pattern of mass homeostasis was robust among different cortical regions, cell types, and experimental conditions and was attributed to an intrinsic homeostatic control mechanism at the cellular level. Maintenance of a form of homeostasis related to spatial mass gradients with age as found in the present study might reflect an analogous intrinsic cellular control mechanism that is conserved in aging.

General Electrotonic Characteristics of Layers II/III Pyramidal Neurons

Similar to previous electrotonic analyses of pyramidal neurons (Mainen et al. 1996; Carnevale et al. 1997; Trevelyan and Jack 2002), we found that attenuation of somatopetal signals (L_{in}) was around an order of magnitude greater than attenuation of somatofugal signals (L_{out}) in both long and local neuron classes (see Fig. 5). The L_{out} transforms were dominated by the thick, proximal apical trunks, whereas the thin, distal branches of both apical and basal dendrites dominated the L_{in} transforms. Thus, the apical trunks appeared to shrink relative to the rest of the dendritic tree, whereas the basal dendrites appeared to grow relative to the rest of the dendritic tree in the L_{in} transforms as compared with the L_{out} transforms, resulting in symmetric passive attenuations for PSPs propagating inward from synapses on either basal or distal apical branches. Because voltage attenuation increases with frequency (for details, see Carnevale et al. 1997), these effects were enhanced at higher frequencies (see Fig. 8).

Effects of Age on Passive Electrotonic Structure

After taking spines into account, aging significantly reduced mean somatopetal ($\bar{L}_{in}$) and somatofugal ($\bar{L}_{out}$) attenuation lengths in apical dendrites of long projection neurons and somatofugal ($\bar{L}_{out}$) attenuation lengths in local projection neurons but did not alter the electrotonic structure of the basal dendrites. These effects remained significant as frequency increased from DC to 500 Hz. The significant reduction in these measures of electrotonic structure with age can be attributed to 2 factors: 1) the reduction in average apical branch length for long projection neurons and 2) the reduction of spine densities for both long and local projection neurons, which will further reduce the effective surface area contributing to electrotonic structure in the aged neurons. These differences were restricted to the apical dendrites; other than at a single frequency point (0 Hz, spine corrected), the electrotonic structure of basal dendrites was unaffected by age in either neuron class. These effects were not surprising in long projection neurons, whose morphometric analysis showed significant reductions in branching and dendritic diameters in aging, but were novel in local projection neurons, for which no significant age-related differences in dendritic structure had previously been reported (Duan et al. 2000). Based on their distribution in the layers II and III and their generally smaller size, local projection neurons correspond to a class of pyramidal cells generally believed to be less vulnerable to the pathological mechanisms that condition neuronal demise in aging and further in neurodegenerative disorders such as Alzheimer's disease (Bussière et al. 2003; for review, see Hof and Morrison 2004).

The significant effects of age on electrotonic structure of local projection neurons found in the present study demonstrate the importance of accurate 3-D reconstructions of dendrite diameters and spines in morphometric studies that attempt to infer function. Unless compensated by altered ion channel densities or distributions, the reduced L_{in} attenuations in apical dendrites of old long projecting neurons will result in less attenuation of dendritic potentials propagating toward the soma, whereas the reduced L_{out} attenuations in both projection types will produce larger, faster peaks of backpropagating APs. The AP backpropagation simulations verified these predictions.

Functional Significance of Reduced Attenuation in Aging

As demonstrated by the backpropagation simulations, the reduced values of $\bar{L}_{out}$ in apical dendrites allow higher backpropagating AP amplitudes along the entire extent of the apical trunk into the apical tuft (Fig. 9). $\bar{L}_{out}$ was a substantially better linear predictor of passive backpropagation efficacy (NBParea) than any of the standard global morphometric measures, such as total membrane surface area or total volume (see Fig. 10), emphasizing the importance of accurate 3-D measures of dendritic diameters and spine densities in making functional inferences from morphometric studies. The roughly 2-fold asymmetry in apical:basal attenuation for somatofugal membrane potentials, such as backpropagating APs, was reduced with age. $\bar{L}_{out}$ attenuation in old neurons more closely resembled the apical:basal symmetry for $\bar{L}_{in}$ attenuation. These changes will affect voltage-dependent mechanisms for synaptic modifications underlying several forms of learning and memory. In particular, backpropagating APs provide a coincidence detection mechanism linking firing in the postsynaptic neuron to presynaptic activity, which triggers synaptic plasticity (Stuart et al. 1997; Linden 1999; Häusser et al. 2000; Waters et al. 2005; Kampa et al. 2006). Studies of spike timing-dependent plasticity (STDP) have shown that the sign and magnitude of synaptic plasticity depend sensitively on the coincidence of a precise temporal window around pre- and postsynaptic potentials (Markram et al. 1997; Zhang et al. 1998; Sjöström et al. 2001). Although more recent work suggests that the mechanism of STDP is more complex than simple coincidence of single backpropagating APs and EPSPs (Lisman and Spruston 2005; Kampa et al. 2006), the contribution of dendritic morphology to the mechanism underlying STDP is well established (for review, see Waters et al. 2005). As a consequence, significant changes in excitatory and inhibitory channel densities along the apical trunk and into apical tufts would be necessary to restore the normal levels of dendritic excitability and the normal spatial integration pattern in old neurons.

In summary, the major effects of age on passive electrotonic structure in both cell classes were in the apical trees. The reduced passive attenuations of somatofugal signals in long and local projection neurons will potentially alter the plasticity mechanisms modulating synaptic strengths in distal regions of apical dendrites that are the major target of excitatory signals from corticocortical, association, and projection neurons (Jones 1975; Rockland and Pandya 1979; Barbas 1986). The reduced passive attenuations of somatopetal signals in long projection neurons, in addition to higher input resistance to somatic current injections, may increase neuronal excitability in aging, resulting in higher firing rates in response to a given dendritic or somatic input (Mainen and Sejnowski 1996;

Kabaso et al. 2004). Both effects could be compensated by changes in active membrane properties: the complex, generally nonlinear interactions between dendritic morphology and synaptic inputs, membrane channel densities, distributions and even kinetics mean that compensation could be achieved by any or many different combinations of these (Goldman et al. 2001; Marder and Prinz 2003; Weaver and Wearne 2008). As a simple example, the shorter electrotonic lengths of old neurons could be compensated by reducing the ratios of either excitatory to inhibitory synaptic inputs in a network context or excitatory to inhibitory membrane conductances in individual cells.

The reduced number of spines in old neurons resulted in a reduction in the voltage attenuation due to passive electrotonic structure that would be expected, in the absence of other effects, to increase the excitability of aged neurons. Interestingly, a recent in vitro electrophysiological study in layers II/III pyramidal cells of area 46 (local projection neurons) reported increased neuronal excitability measured by firing rates and increased input resistance in response to somatic current injections (Chang et al. 2005). The presence of fewer spines also implies a potential decrease in dendritic input that might reduce the excitatory drive on the cell. A related study reported that the frequency of excitatory postsynaptic currents was reduced, and the frequency of inhibitory postsynaptic currents was increased with age in these same area 46 neurons (Luebke et al. 2004). The altered synaptic input may represent a compensatory mechanism to reduce excitability resulting from age-related reductions in passive electrotonic structure. Although we found reduced mean attenuations only for somatofugal signals in local projection neurons, we do report a nonsignificant ($P = 0.21$) decrease of 7.4% in somatopetal attenuation for the manually traced dataset of this study. The high measurement variability inherent in hand-traced neurons (Scorcioni et al. 2004), together with absence of information on spine geometries, may have prevented us from resolving a significant difference. Our current research is addressing this issue using automated tracing methods that reduce these and other sources of measurement error (Rodriguez et al. 2003, 2008).

Implications for Cognitive Function

Neurons of the PFC encode information in working memory tasks through precisely tuned, sustained alterations in AP firing rates during the delay epoch of a working memory task (Funahashi et al. 1989; Goldman-Rakic 1995; Constantinidis et al. 2001). Unless compensated by changes in passive cable parameters (*Rm*, *Ra*, and *Cm*), active membrane properties or synaptic properties, the reduced passive attenuations of both somatopetal and somatofugal signals will increase neuronal excitability in aging, resulting in higher firing rates in response to a given somatic or synaptic input (Mainen and Sejnowski 1996; Kabaso et al. 2004). Consequent changes in signal propagation to the dendrites could affect STDP, altering synaptic strengths and potentially compromising the networks' ability to maintain the robust persistent activity that underlies working memory. Alterations in the mean frequency or precise spike timing of AP trains as a result of the significantly altered electrotonic structure of long projection neurons providing afferent input to working memory networks of the PFC could similarly compromise the ability to maintain persistent activity in those networks, ultimately resulting in impaired cognitive performance.

It is increasingly evident that in the absence of overt neurobiological changes such as neuron loss in aging, more subtle structural changes at the single-cell level may explain age-related cognitive decline. This study reveals substantial functional consequences of reduced membrane surface area resulting from loss of spines, altered dendritic diameters, and reduced branching complexity in neurons contributing to PFC circuits. These functional consequences may account for the cognitive and behavioral deficits commonly seen in aged macaque monkeys (Gallagher and Rapp 1997; Herndon et al. 1997; Chang et al. 2005) as well as in normal human brain aging (Albert 1997; Grady and Craik 2000; Grady et al. 2003; Grady 2008).

Funding

NIH (DC05669 and MH71818 to S.L.W.; MH58911 and AG05138 and AG02219 to P.R.H) and Australian Research Council Discovery (DP0665482 to B.I.H. and S.L.W.).

Notes

The authors thank Alfredo Rodriguez and Douglas Ehlenberger for technical assistance with image analysis and morphometry software, Kevin Kelliher for hardware assistance, and all the colleagues in the Wearne and Hof laboratories for their ongoing participation. Thanks also to Ted Carnevale and Michael Hines for many discussions and ongoing guidance in the use of NEURON. Special thanks are due to Dr Huiling Duan, who traced the original dataset of 80 pyramidal neurons, and to Dr Jennifer I. Luebke for providing the electrophysiological data for performing the backpropagation simulations and for the spectral analysis used to determine physiologically relevant frequency ranges for the electrotonic transforms. *Conflict of Interest*: None declared.

Address correspondence to Email: susan.wearne@mssm.edu.

APPENDIX I: Definition of Scaling Exponents

By assuming that intracellular mass per unit volume is uniform, mass scaling is measured from the change in total dendritic volume with distance. For a dendritic structure of mass $M(x)$ that extends a distance x from the soma in dendrogram space (see definition below), the mass scaling exponent d_M was defined by the scaling relation

$$M(x) \sim x^{d_M}, \tag{A1.1}$$

where equation (A1.1) assumes that $|M(x)/x^{d_M}|$ remains constant over a range of values of x, defined as the scaling region (Rothnie et al. 2006). Accumulated mass $M(x)$ of a dendritic tree is measured as a function of distance x in dendrogram space from the total cross-sectional area of intersection of the tree with a sequence of parallel planes, orthogonal to the "stretched out" branches. The exponent d_M is simply measured from experimental data as the slope of the graph of log(accumulated mass) versus log(x). In dendrogram space, we can uncouple the contributions of branching and tapering to mass scaling, as follows. The incremental mass, $dM(x)$, between planes in dendrogram space at x and dx scales as

$$\mathrm{d}M(x) \sim x^{d_M - 1}\mathrm{d}x, \tag{A1.2}$$

and thus the total cross-sectional area of intersection of the dendritic tree with these planes, $S(x)$, scales as

$$S(x) \sim x^{d_A}, \tag{A1.3}$$

where the scaling exponent d_A is equal to $d_M - 1$, reflecting the spatial derivative relationship between the quantities $S(x)$ and $M(x)$. Analogously, the branching exponent d_N is defined by a scaling law for the

number of branch intersections $N(x)$ with sequential planes at distance x, orthogonal to the long axis of the branches

$$N(x) \sim x^{d_N}, \tag{A1.4}$$

and the tapering exponent d_T is defined by a scaling law for the average branch area of intersection, $<S(x)>$, with those sequential planes:

$$<S(x)> \sim x^{d_T}. \tag{A1.5}$$

Because dendritic branches usually taper with distance from the soma, the tapering exponents are generally negative, whereas the branching exponent can be positive or negative depending on whether dendrites branch or die-off. The following theoretical relationships were obtained between the scaling exponents: the mass exponent is equal to the area exponent plus one (Rothnie et al. 2006)

$$d_M = d_A + 1, \tag{A1.6}$$

and the area exponent is the sum of tapering and branching exponents

$$d_A = d_T + d_N. \tag{A1.7}$$

Dendrogram space: In accordance with the theory developed in Rothnie et al. (2006), we measured all scaling exponents in dendrogram space. The important parameters in electrotonic cable models of neurons are lengths, diameters, and branching of dendrites, which can be represented in a schematic dendrogram of the neuronal morphology as a binary tree (e.g., basal tree of young neuron drawn in Fig. 3*C*; apical tree of old neuron drawn in Fig. 3*F*). In dendrogram space, the branches are stretched out and aligned with the single axis of the space (the vertical axis in Fig. 3). The arclength of the root branch is represented as a distance along this primary axis. The arclengths of progeny branches are represented as lengths in a direction parallel to the same primary axis, starting at a distance given by the arclength from the root to their branchpoints of origin. An important feature of the dendrogram space representation is that the distance metric is proportional to the arclength along dendritic branches, which determines their cable properties. A second important feature is that the cross-sections of branches with sequential parallel planes placed orthogonal to their primary axes will always be circular, simplifying the computation of cross-sectional area of intersection, used in the scaling exponents d_A and d_T.

APPENDIX II: Computation of Attenuation Measures

$\bar{L}$: mean attenuation

For a steady state voltage stimulus at the soma, the logarithm of somatofugal voltage attenuation (L_{out}) is defined at a given point j in the dendritic tree

$$L_{out} = \ln\frac{V_s}{V_j}, \tag{A2.1}$$

where V_s is the somatic voltage and V_j is the voltage measured by a theoretical electrode at point j. Equivalently, somatopetal voltage attenuation (L_{in}) is defined at each point for a voltage stimulus at that point, measured at the soma

$$L_{in} = \ln\frac{V_j}{V_s}. \tag{A2.2}$$

Note that $L_{out} \neq 1/L_{in}$ because the positions of the hypothetical stimulus and recording electrode are reversed. L_{out} and L_{in} are defined at every point in the dendritic tree, so they can be analyzed as functions of arclength s along unbranched dendrite. For purposes of analysis, we define $L_k(s_i)$ as the attenuation value (outward or inward) at each compartment s_i on the unbranched section k of the dendritic tree composed of K distinct unbranched sections.

The function average of $L_k(s)$ over a given unbranched section k with total arclength x_k is

$$\bar{L}_k = \frac{1}{x_k}\int_0^{x_k} L_k(s)\ ds. \tag{A2.3}$$

Taking the average over all K sections gives

$$\bar{L} = \left(1 \Big/ \sum_{k=1}^{K} x_k\right)\left[\sum_{k=1}^{K}\left(\int_0^{x_k} L_k(s)\ ds\right)\right]. \tag{A2.4}$$

In practice, attenuation is only computed by NEURON for a finite number of discrete compartments, using a discretized form of the cable equation (Carnevale and Hines 2006). Therefore, the integral in equation (A2.4) is replaced with a Riemann sum

$$\bar{L} = \left(1 \Big/ \sum_{k=1}^{K} x_k\right)\left[\sum_{k=1}^{K}\left(\sum_{i=1}^{I} L_k(s_{i,k})\ \Delta s_{i,k}\right)\right], \tag{A2.5}$$

where the sum is taken over the I compartments of each unbranched section and $\Delta s_{i,k}$ is the arclength of the ith compartment of the kth unbranched section. To eliminate discretization effects, the number of compartments used in the model neuron was increased until the mean attenuation value converged.

The Riemann sum can be simplified by noting that the sums iterate over every compartment in the neuron exactly once. For a dendritic tree with J compartments, the sum simplifies to

$$\bar{L} = \left(1 \Big/ \sum_{j=1}^{J} \Delta s_j\right)\ \left[\sum_{j=1}^{J} L_j(s_j)\,\Delta s_j\right]. \tag{A2.6}$$

Formally, this is identical to the weighted average of the per-compartment log attenuation L_j, weighted by the arclength s_j of each compartment.

The connection between equation (A2.6) and the function average of attenuation along each branch provides a rationale for computing L_{out} and L_{in} as weighted averages normalized by arclength. However, an alternative approach, used by Bui et al. (2003), is to perform the weighting according to surface area, which gives the sample mean of attenuation at synapses, if synapses are assumed to be distributed evenly over the dendritic membrane. In this formulation,

$$\bar{L}_a = \frac{\sum_{j=1}^{J} L_j(s_j)\ \Delta a_j}{\sum_{j=1}^{J} \Delta a_j}, \tag{A2.7}$$

where L_a is the mean surface area-normalized attenuation and Δa_j is the surface area of each dendritic compartment j.

This formulation is applicable to somatopetal or somatofugal log voltage attenuation (L_{in} or L_{out}), so long as the corresponding measure of attenuation (inward or outward) is used.

NBParea: normalized backpropagation area:

The NBParea, Y, of a dendritic tree is defined by

$$Y = \frac{1}{x}\int_0^x \bar{V}(s)\ ds, \tag{A2.8}$$

where $\bar{V}(s)$ is the average AP backpropagation potential as a function of branch arclength s (averaged across different branches at the same distance), x is the maximum soma-to-tip branch distance, and Y is the function average of $\bar{V}(s)$ on the domain $s \in [0, x]$.

An interesting relationship can be demonstrated between Y (NBParea) and $\bar{L}_{out}$. Along an unbranched stretch of passive dendrite, voltage decays exponentially with distance according to the space constant λ,

$$V(s) = V_s e^{-x\lambda}. \tag{A2.9}$$

For $\bar{V}_s$, the relationship is only approximate due to the voltage effects of sealed dendritic tips and the fact that $\bar{V}(s)$ is an average of voltage over multiple branches. For some constant λ,

$$\bar{V}(s) \approx V_s e^{-x\lambda}. \tag{A2.10}$$

Recall that V_s is the voltage at the soma. Equation (A2.8) can now be integrated:

$$Y \approx \frac{\lambda V_s}{x}\left(1 - e^{-x\lambda}\right), \tag{A2.11}$$

which if $x \Big/ \lambda >> 1$ implies

$$Y \sim \frac{\lambda V_s}{x}. \tag{A2.12}$$

Combine equation (A2.1) with equation (A2.6):

$$\bar{L} = \frac{\sum_{j=1}^{J} \Delta s_j \ln\left(V_s / V_j\right)}{\sum_{j=1}^{J} \Delta s_j}, \tag{A2.13}$$

$$= \frac{1}{S} \sum_{j=1}^{J} \Delta s_j \ln\left(V_s \Big/ V_j\right), \tag{A2.14}$$

where S is the total arclength of all dendritic branches. The sum will be dominated by contributions where attenuation is greatest, that is, by contributions from the most distant nodes where s is close to the maximum branch length x (if $V_s \approx V_j$ then $\ln\left(V_s / V_j\right) \approx 0$) and thus

$$\bar{L} \sim \frac{\Delta s_x}{S} \ln \frac{V_s}{V(x)}. \tag{A2.15}$$

From equation (A2.9),

$$\frac{V_s}{V(x)} \approx \exp\left(\frac{x}{\lambda}\right). \tag{A2.16}$$

and so

$$\bar{L} \sim \frac{x \Delta s_x}{\lambda S}. \tag{A2.17}$$

Combining equations (A2.12) and (A2.17) gives:

$$Y \sim \frac{V_0 \Delta s_x}{\bar{L}}, \tag{A2.18}$$

$$\bar{L} \sim \frac{1}{Y}. \tag{A2.19}$$

Thus, in a log-log plot of NBParea versus $\bar{L}_{\text{out}}$, a roughly linear relation with a negative slope is expected. This is only a leading approximation, but it contributes to a physical understanding of the high linear correlation between ln(NBParea) and $\ln(\bar{L}_{\text{out}})$ shown in Figure 10*A*.

References

Albert MS. 1997. The ageing brain: normal and abnormal memory. Philos Trans R Soc Lond B Biol Sci. 352:1703–1709.

Bachevalier J, Landis LS, Walker LC, Brickson M, Mishkin M, Price DL, Cork LC. 1991. Aged monkeys exhibit behavioral deficits indicative of widespread cerebral dysfunction. Neurobiol Aging. 12:99–111.

Barbas H. 1986. Pattern in the laminar origin of corticocortical connections. J Comp Neurol. 252:415–422.

Brown TH, Zador A, Mainen ZF, Claiborne BJ. 1992. Hebbian computations in hippocampal dendrites and spines. In: McKenna T, Davis J, Zornetzer SF, editors. Single neuron computation. San Diego (CA): Academic Press. p. 81–116.

Bui TV, Cushing S, Dewey D, Fyffe RE, Rose PK. 2003. Comparison of the morphological and electrotonic properties of Renshaw cells, Ia inhibitory interneurons, and motoneurons in the cat. J Neurophysiol. 90:2900–2918.

Burke RE. 2000. Comparison of alternative designs for reducing complex neurons to equivalent cables. J Comput Neurosci. 9:31–47.

Bussière T, Giannakopoulos P, Bouras C, Perl DP, Morrison JH, Hof PR. 2003. Progressive degeneration of nonphosphorylated neurofilament protein-enriched pyramidal neurons predicts cognitive impairment in Alzheimer's disease: a stereologic analysis of prefrontal cortex area 9. J Comp Neurol. 463:281–302.

Carnevale NT, Hines ML. 2006. The NEURON book. Cambridge (UK): Cambridge University Press.

Carnevale NT, Tsai KY, Claiborne BJ, Brown TH. 1997. Comparative electrotonic analysis of three classes of rat hippocampal neurons. J Neurophysiol. 78:703–720.

Caserta F, Eldred WD, Fernandez E, Hausman RE, Stanford LR, Bulderev SV, Schwarzer S, Stanley HE. 1995. Determination of fractal dimension of physiologically characterized neurons in two and three dimensions. J Neurosci Methods. 56:133–144.

Chang YM, Rosene DL, Killiany RJ, Mangiamele LA, Luebke JI. 2005. Increased action potential firing rates of layer 2/3 pyramidal cells in the prefrontal cortex are significantly related to cognitive performance in aged monkeys. Cereb Cortex. 15:409–418.

Constantinidis C, Franowicz MN, Goldman-Rakic PS. 2001. Coding specificity in cortical microcircuits: a multiple-electrode analysis of primate prefrontal cortex. J Neurosci. 21:3646–3655.

de Brabander JM, Kramers RJ, Uylings HB. 1998. Layer-specific dendritic regression of pyramidal cells with ageing in the human prefrontal cortex. Eur J Neurosci. 10:1261–1269.

de Lima AD, Voigt T, Morrison JH. 1990. Morphology of the cells within the inferior temporal gyrus that project to the prefrontal cortex in the macaque monkey. J Comp Neurol. 296:159–172.

Dickstein DL, Kabaso D, Rocher AB, Luebke JI, Wearne SL, Hof PR. 2007. Changes in the structural complexity of the aged brain. Aging Cell. 6:275–284.

Duan H, He Y, Wicinski B, Morrison JH, Hof PR. 2000. Age-related dendrite and spine changes in corticocortically projecting neurons in macaque monkeys. Soc Neurosci Abstr. 26:1237.

Duan H, Wearne SL, Morrison JH, Hof PR. 2002. Quantitative analysis of the dendritic morphology of corticocortical projection neurons in the macaque monkey association cortex. Neuroscience. 114:349–359.

Duan H, Wearne SL, Rocher AB, Macedo A, Morrison JH, Hof PR. 2003. Age-related morphologic alterations in dendrites and spine densities of corticocortically projecting neurons in macaque monkeys. Cereb Cortex. 13:950–961.

Durstewitz D, Seamans JK, Sejnowski TJ. 2000. Neurocomputational models of working memory. Nat Neurosci. 3:1184–1191.

Flicker C, Ferris SH, Crook TH, Bartus RT. 1987. A visual recognition memory test for the assessment of cognitive function in aging and dementia. Exp Aging Res. 13:127–132.

Fristoe NM, Salthouse TA, Woodard JL. 1997. Examination of age-related deficits on the Wisconsin Card Sorting Test. Neuropsychology. 11:428–436.

Funahashi S, Bruce CJ, Goldman-Rakic PS. 1989. Mnemonic coding of visual space in the primate dorsolateral prefrontal cortex. J Neurophysiol. 61:331–349.

Funahashi S, Kubota K. 1994. Working memory and prefrontal cortex. Neurosci Res. 21:1–11.

Fuster J. 1997. Network memory. Trends Neurosci. 10:451–459.

Gallagher M, Rapp PR. 1997. The use of animal models to study the effects of aging on cognition. Annu Rev Psychol. 48:339–370.

Gazzaley AH, Thakker MM, Hof PR, Morrison JH. 1997. Preserved number of entorhinal cortex layer II neurons in aged macaque monkeys. Neurobiol Aging. 18:549–553.

Goldman MS, Golowasch J, Marder E, Abbott LF. 2001. Global structure, robustness, and modulation of neuronal models. J Neurosci. 21:5229–5238.

Goldman-Rakic PS. 1988. Topography of cognition: parallel distributed networks in primate association cortex. Annu Rev Neurosci. 11:137–156.

Goldman-Rakic PS. 1995. Cellular basis of working memory. Neuron. 14:477–485.

Goldman-Rakic PS. 1996. Regional and cellular fractionation of working memory. Proc Natl Acad Sci USA. 93:13473–13480.

Grady CL. 2008. Cognitive neuroscience of aging. Ann N Y Acad Sci. 1124:127–144.

Grady CL, Craik FIM. 2000. Changes in memory processing with age. Curr Opin Neurobiol. 10:224–231.

Grady CL, McIntosh AR, Beig S, Keightley ML, Burian H, Black SE. 2003. Evidence from functional neuroimaging of a compensatory prefrontal network in Alzheimer's disease. J Neurosci. 23:986–993.

Häusser M, Spruston N, Stuart G. 2000. Diversity and dynamics of dendritic signaling. Science. 290:739–744.

Henry BI, Hof PR, Rothnie P, Wearne SL. 2002. Fractal analysis of aggregates of non-uniformly sized particles: an application to macaque monkey cortical pyramidal neurons. In: Novak MM, editor. Emergent nature: patterns, growth and scaling in the sciences. Singapore: World Scientific Publishing. p. 65–75.

Herndon JG, Moss MB, Rosene D, Killiany RJ. 1997. Patterns of cognitive decline in aged rhesus monkeys. Behav Brain Res. 87:25–35.

Hines ML. 1994. The NEURON simulation program. In: Skrzypek J, editor. Neural network simulation environments. Norwell (MA): Kluwer. p. 147–163.
Hof PR, Cox K, Morrison JH. 1990. Quantitative analysis of a vulnerable subset of pyramidal neurons in Alzheimer's disease. I. Superior frontal and inferior temporal cortex. J Comp Neurol. 301:44–54.
Hof PR, Morrison JH. 2004. The aging brain: morphomolecular senescence of cortical circuits. Trends Neurosci. 27:607–613.
Hof PR, Nimchinsky EA, Morrison JH. 1995. Neurochemical phenotype of corticocortical connections in the macaque monkey: quantitative analysis of a subset of neurofilament protein-immunoreactive projection neurons in frontal, parietal, temporal and cingulate cortices. J Comp Neurol. 362:109–133.
Hof PR, Nimchinsky EA, Young WG, Morrison JH. 2000. Numbers of Meynert and layer IVB cells in area V1: a stereologic analysis in young and aged macaque monkeys. J Comp Neurol. 420:113–126.
Jelinek HF, Elston GN. 2001. Pyramidal neurones in macaque visual cortex: interareal phenotypic variation of dendritic branching patterns. Fractals. 9:297–303.
Jones EG. 1975. Varieties and distribution of non-pyramidal cells in the somatic sensory cortex of the squirrel monkey. J Comp Neurol. 160:205–267.
Kabaso D, Luebke JI, Henry BI, Hof PR, Wearne SL. 2004. Morphologic changes in dendritic structure and spine densities may account for age-related increases in action potential firing rates. Program Number: 638.18. Washington (DC): Society for Neuroscience.
Kampa BM, Letzkus JJ, Stuart GJ. 2006. Requirement of dendritic calcium spikes for induction of spike-timing-dependent synaptic plasticity. J Physiol. 574:283–290.
Kritzer MF, Goldman-Rakic PS. 1995. Intrinsic circuit organization of the major layers and sublayers of the dorsolateral prefrontal cortex in the rhesus monkey. J Comp Neurol. 359:131–143.
Larkman AU, Major G, Stratford KJ, Jack JJ. 1992. Dendritic morphology of pyramidal neurones of the visual cortex of the rat. IV: electrical geometry. J Comp Neurol. 323:137–152.
Levitt JB, Lewis DA, Yoshioka T, Lund JS. 1993. Topography of pyramidal neuron intrinsic connections in macaque monkey prefrontal cortex (areas 9 and 46). J Comp Neurol. 338:360–376.
Levy R, Goldman-Rakic PS. 2000. Segregation of working memory functions within the dorsolateral prefrontal cortex. Exp Brain Res. 133:23–32.
Lewis DA, Melchitzky DS, Burgos GG. 2002. Specificity in the functional architecture of primate prefrontal cortex. J Neurocytol. 31:265–276.
Linden DJ. 1999. The return of the spike: postsynaptic action potentials and the induction of LTP and LTD. Neuron. 22:661–666.
Lisman JE, Fellous JM, Wang XJ. 1998. A role for NMDA-receptor channels in working memory. Nat Neurosci. 1:273–275.
Lisman JE, Spruston N. 2005. Postsynaptic depolarization requirements for LTP and LTD: a critique of spike timing-dependent plasticity. Nat Neurosci. 8:839–841.
Luebke JI, Chang YM, Moore TL, Rosene DL. 2004. Normal aging results in decreased synaptic excitation and increased synaptic inhibition of layer 2/3 pyramidal cells in the monkey prefrontal cortex. Neuroscience. 125:277–288.
Mainen ZF, Carnevale NT, Zador A, Claiborne BJ. 1996. Electrotonic architecture of hippocampal CA1 pyramidal neurons based on three-dimensional reconstructions. J Neurophysiol. 76:1904–1923.
Mainen ZF, Sejnowski TJ. 1996. Influence of dendritic structure on firing pattern in model neocortical neurons. Nature. 382:363–366.
Major G, Evans JD, Jack JJB. 1993. Solutions for transients in arbitrarily branching cables: I. Voltage recording with a somatic shunt. Biophys J. 65:423–449.
Marder E, Prinz AA. 2003. Current compensation in neuronal homeostasis. Neuron. 37:2–4.
Markram H, Lübke J, Frotscher M, Sakmann B. 1997. Regulation of synaptic efficacy by coincidence of postsynaptic APs and EPSPs. Science. 275:213–215.
Melchitzky DS, Sesack SR, Pucak ML, Lewis DA. 1998. Synaptic targets of pyramidal neurons providing intrinsic horizontal connections in monkey prefrontal cortex. J Comp Neurol. 390:211–224.
Miller EK, Cohen JD. 2001. An integrative theory of prefrontal cortex function. Annu Rev Neurosci. 24:167–202.
Miller EK, Erickson CA, Desimone R. 1996. Neural mechanisms of visual working memory in prefrontal cortex of the macaque. J Neurosci. 16:5154–5167.
Morrison JH, Hof PR. 1997. Life and death of neurons in the aging brain. Science. 278:412–419.
Nimchinsky EA, Hof PR, Young WG, Morrison JH. 1996. Neurochemical, morphologic and laminar characterization of cortical projection neurons in the cingulate motor areas of the macaque monkey. J Comp Neurol. 374:136–160.
O'Donnell KA, Rapp PR, Hof PR. 1999. The volume of prefrontal cortex area 46 is preserved during aging in macaque monkeys. Exp Neurol. 160:300–310.
Peters A, Morrison JH, Rosene D, Hyman BT. 1998. Are neurons lost from the primate cerebral cortex during normal aging? Cereb Cortex. 8:295–300.
Pucak ML, Levitt JB, Lund JS, Lewis DA. 1996. Patterns of intrinsic and associational circuitry in monkey prefrontal cortex. J Comp Neurol. 376:614–630.
Rall W. 1959. Branching dendritic trees and motoneuron resistivity. Exp Neurol. 1:491–527.
Rall W. 1962. Theory of physiological properties of dendrites. Ann N Y Acad Sci. 96:1071–1092.
Rall W. 1969. Time constants and electrotonic length of membrane cylinders and neurons. Biophys J. 9:1483–1508.
Rapp PR, Amaral DG. 1989. Evidence for task-dependent memory dysfunction in the aged monkey. J Neurosci. 9:3568–3576.
Rice JA. 2006. Mathematical statistics and data analysis. Pacific Grove (CA): Duxbury Press.
Rockland KS, Pandya DN. 1979. Laminar origins and terminations of cortical connections of the occipital lobe in the rhesus monkey. Brain Res. 179:3–20.
Rodriguez A, Ehlenberger DB, Dickstein DL, Hof PR, Wearne SL. 2008. Automated three-dimensional detection and shape classification of dendritic spines from fluorescence microscopy images. PLoS ONE. 3(4):e1997.
Rodriguez A, Ehlenberger D, Hof PR, Wearne SL. 2006. Rayburst sampling, an algorithm for automated three-dimensional shape analysis from laser-scanning microscopy images. Nat Protoc. 1:2156–2161.
Rodriguez A, Ehlenberger D, Kelliher KT, Einstein M, Henderson SC, Morrison JH, Hof PR, Wearne SL. 2003. Automated reconstruction of three-dimensional neuronal morphology from laser scanning microscopy images. Methods. 30:94–105.
Rothnie P, Kabaso D, Hof PR, Henry BI, Wearne SL. 2006. Functionally relevant measures of spatial complexity in neuronal dendritic arbors. J Theor Biol. 238:506–526.
Samsonovich AV, Ascoli GA. 2006. Morphological homeostasis in cortical dendrites. Proc Natl Acad Sci USA. 103:1569–1574.
Scorcioni R, Lazarewicz MT, Ascoli GA. 2004. Quantitative morphometry of hippocampal pyramidal cells: differences between anatomical classes and reconstructing laboratories. J Comp Neurol. 473(2): 177–193.
Shimada A, Tsuzuki M, Keino H, Satoh M, Chiba Y, Saitoh Y, Hosokawa M. 2006. Apical vulnerability to dendritic retraction in prefrontal neurones of ageing SAMP 10 mouse: a model of cerebral degeneration. Neuropathol Appl Neurobiol. 32:1–14.
Sholl DA. 1953. Dendritic organization in the neurons of the visual and motor cortices of the cat. J Anat. 87:387–406.
Sjöström PJ, Turrigiano GG, Nelson SB. 2001. Rate, timing, and cooperativity jointly determine cortical synaptic plasticity. Neuron. 32:1149–1164.
Smith TG, Marks WB, Lange GD, Sheriff JWH, Neale EA. 1989. A fractal analysis of cell images. J Neurosci Methods. 27:173–180.
Stern Y, Zarahn E, Habeck C, Holtzer R, Rakitin BC, Kumar A, Flynn J, Steffener J, Brown T. 2008. A common neural network for cognitive reserve in verbal and object working memory in young but not old. Cereb Cortex. 18:959–967.
Stratford K, Mason A, Larkman A, Major G, Jack J. 1989. The modeling of pyramidal neurons in the visual cortex. In: Durbin R, Miall C, Mitchison G, editors. The computing neuron. London: Addison-Wesley. p. 296–321.
Stuart G, Spruston N. 1998. Determinants of voltage attenuation in neocortical pyramidal neuron dendrites. J Neurosci. 18:3501–3510.

Stuart G, Spruston N, Sakmann B, Häusser M. 1997. Action potential initiation and backpropagation in neurons of the mammalian CNS. Trends Neurosci. 20:125–131.

Trevelyan AJ, Jack J. 2002. Detailed passive cable models of layer 2/3 pyramidal cells in rat visual cortex at different temperatures. J Physiol. 593:623–636.

Tsai KY, Carnevale NT, Claiborne BJ, Brown TH. 1994. Efficient mapping from neuroanatomical to electrotonic space. Networks. 5:21–46.

Van der Gucht E, Youakim M, Arckens L, Hof PR, Baizer JS. 2006. Variations in the structure of the prelunate gyrus of Old World monkeys. Anat Rec. 288:753–775.

Wang XJ. 2001. Synaptic reverberation underlying mnemonic persistent activity. Trends Neurosci. 24:455–463.

Waters J, Schaefer A, Sakmann B. 2005. Backpropagating action potentials in neurones: measurement, mechanisms and potential functions. Prog Biophys Mol Biol. 87:145–170.

Wearne SL, Rodriguez A, Ehlenberger D, Rocher AB, Henderson SC, Hof PR. 2005. New techniques for imaging, digitization and analysis of three-dimensional neuronal morphology on multiple scales. Neuroscience. 136:661–680.

Weaver CM, Wearne SL. 2008. Neuronal firing sensitivity to morphologic and active membrane parameters. PLoS Comput Biol. 4(1):e11.

West MJ, Coleman PD, Flood DG, Troncoso JC. 1994. Differences in the pattern of hippocampal neuronal loss in normal aging and Alzheimer's disease. Lancet. 344:769–772.

Zador AM, Agmon-Snir H, Segev I. 1995. The morphoelectrotonic transform: a graphical approach to dendritic function. J Neurosci. 15:1669–1682.

Zhang LI, Tao HW, Holt CE, Harris WA, Poo MM. 1998. A critical window for cooperation and competition among developing retinotectal synapses. Nature. 395:37–44.